

Constraining the structure and formation of the Galactic bulge from a field in its outskirts[★]

FLAMES-GIRAFFE spectra of about 400 red giants around $(l, b) = (0^\circ, -10^\circ)$

S. Uttenthaler¹, M. Schultheis^{2,3}, D. M. Nataf⁴, A. C. Robin², T. Lebzelter¹, and B. Chen²

¹ University of Vienna, Department of Astronomy, Türkenschanzstraße 17, 1180 Vienna, Austria
e-mail: stefan.uttenthaler@univie.ac.at; thomas.lebzelter@univie.ac.at

² Institut Utinam, CNRS UMR6213, OSU THETA, Université de Franche-Comté, 41bis avenue de l'Observatoire, 25000 Besançon, France

e-mail: mathias@obs-besancon.fr; annie.robin@obs-besancon.fr

³ Institut d'Astrophysique de Paris, UMR 7095 CNRS, Université Pierre et Marie Curie, 98bis boulevard Arago, 75014 Paris, France

⁴ Department of Astronomy, Ohio State University, 140 West 18th Avenue, Columbus, OH 43210, USA
e-mail: nataf@astronomy.ohio-state.edu

Received 16 February 2012; accepted 30 July 2012

ABSTRACT

Context. The presence of two stellar populations in the Milky Way bulge have been reported recently, based on observations of giant and dwarf stars in the inner and intermediate bulge.

Aims. We aim at studying the abundances and kinematics of stars in the outer Galactic bulge, thereby providing additional constraints on formation models of the bulge.

Methods. Spectra of 401 red giant stars in a field at $(l, b) = (0^\circ, -10^\circ)$ were obtained with the FLAMES-GIRAFFE spectrograph at the VLT. Stars of luminosities down to below the two bulge red clumps are included in the data set. From these spectra we measure general metallicities, abundances of iron and the α -elements, and radial velocities of the stars. The abundances are derived from an interpolation and fitting procedure within a grid of COMARCS model atmospheres and spectra. These measurements as well as photometric data are compared to simulations with the Besançon and TRILEGAL models of the Galaxy.

Results. We confirm the presence of two populations among our sample stars: i) a metal-rich one at $[M/H] \sim +0.3$, comprising about 30% of the sample, with low velocity dispersion and low α -abundance, and ii) a metal-poor population at $[M/H] \sim -0.6$ with high velocity dispersion and high α -abundance. The metallicity difference between the two populations, a systematically and statistically robust figure, is $\Delta[M/H] = 0.87 \pm 0.03$. The metal-rich population could be connected to the Galactic bar. We identify this population as the carrier of the double red clump feature. We do not find a significant difference in metallicity or radial velocity between the two red clumps, a small difference in metallicity being probably due to a selection effect and contamination by the metal-poor population. The velocity dispersion agrees well with predictions of the Besançon Galaxy model, but the metallicity of the “thick bulge” model component should be shifted to lower metallicity by 0.2 to 0.3 dex to well reproduce the observations. We present evidence that the metallicity distribution function depends on the evolutionary state of the sample stars, suggesting that enhanced mass loss preferentially removes metal-rich stars. We also confirm the decrease of α -element over-abundance with increasing metallicity.

Conclusions. Our sample is consistent with the existence of two populations, one being a metal-rich bar, the second one being more like a metal-poor classical bulge with larger velocity dispersion.

Key words. Galaxy: bulge – Galaxy: formation – Galaxy: kinematics and dynamics – Stars: abundances – Stars: late-type

1. Introduction

The bulge of the Milky Way galaxy is such a complex system that its formation and evolution is still poorly understood. There exist two main scenarios for the Galactic bulge (GB) formation. The first one, called the “classical” scenario, describes the bulge formation through initial collapse of gas at early times (Eggen et al., 1962) or through hierarchical merging of sub-clumps (Noguchi, 1999; Aguerrí et al., 2001). In the monolithic collapse case the bulge formed *before* the disc and the

star-formation time-scale was very short (~ 0.5 Gyr; Thomas et al., 2005). The resulting stars are old ($\gtrsim 10$ Gyr) and have enhancements of α -elements relative to iron in a large range of Fe abundances, which are characteristic of classical bulges. This indicates a very fast bulge formation, where SNe Ia did not have time to pollute the gas with α -element-free ejecta. In the hierarchical merging the bulge also formed before the disc but on a longer timescale (of the order of a few Gyr; Noguchi, 1999) and therefore this approach predicts lower over-abundances of α -elements.

The second scenario, called the “pseudo-bulge” scenario, describes the bulge formation by the buckling of the disc, following a disc instability (also called a bar; Combes et al., 1990; Raha et al., 1991; Norman et al., 1996; Kormendy & Kennicutt, 2004; Athanassoula, 2005). In this case the bulge forms *after* the disc

[★] Based on observations at the Very Large Telescope of the European Southern Observatory, Cerro Paranal/Chile under Programme 083.D-0046(A). Table 3 is only available in electronic form at the CDS via anonymous ftp to cdsarc.u-strasbg.fr (130.79.128.5) or via <http://cdsweb.u-strasbg.fr/cgi-bin/qcat?J/A+A/>.

and on a much longer timescale than a classical bulge. After the bar formation the disc is heated in vertical direction (Combes & Sanders, 1981), giving rise to the typical boxy/peanut shape. The bulge formed in this way will be a mixture of disc stars and stars formed in situ by gas which is likely to be well mixed by the action of the bar. In this scenario, the enhancement of the α -elements in the bulge stars is predicted to be low, similar to that of the inner disc stars in the models.

It should be noted that, in addition to the classical bulge and pseudo-bulge classifications, an alternative formation mechanism has been suggested, namely the “clump-origin bulge”. In this scenario, first proposed by Noguchi (1998) and recently elaborated upon by Inoue & Saitoh (2011), stellar clumps spontaneously form in high gas-density disc galaxies, as shown by N-body/SPH simulations, and dynamical friction drags these clumps to the centre of the galaxy where they aggregate into a bulge-like structure. The models of Inoue & Saitoh (2011) reproduce the observed boxy shape, rapid star formation, and vertical metallicity gradients observed in the bulge of the Milky Way. Clumpy galaxies that could be the analogues of the primordial Milky Way and that are consistent with these models have been observed in the high-redshift universe (Elmegreen & Elmegreen, 2005; Genzel et al., 2011), but also locally (Elmegreen et al., 2012).

Each of these scenarios is supported by at least some of the observational constraints. The question of formation history is crucial and necessary to investigate because our Galaxy is a benchmark for understanding the formation of disc galaxies. Recently, Babusiaux et al. (2010) and Hill et al. (2011) analysed large samples of red clump stars in Baade’s window and three fields close to the minor axis, at $b \sim -4^\circ$, -6° , and -12° , which revealed the presence of two distinct populations: a metal-poor component around $[\text{Fe}/\text{H}] \approx -0.3$ dex with a broad distribution in $[\text{Fe}/\text{H}]$, and metal-rich component centered around $[\text{Fe}/\text{H}] \approx +0.3$ with a small spread in metallicity. In addition, these two populations show kinematical differences: the metal-poor component is compatible with an old spheroid, whereas the metal-rich component is consistent with a bar population. Therefore, two different formation scenarios have been proposed: A rapid formation timescale for the metal-poor component, and a formation over a longer timescale driven by the evolution of the bar (pseudo-bulge) for the metal-rich component. Similarly, Bensby et al. (2011) find two populations in their sample of micro-lensed bulge dwarf and sub-giant stars, centred at $[\text{Fe}/\text{H}] \approx -0.6$ and $[\text{Fe}/\text{H}] \approx +0.3$, with a dearth of stars around $[\text{Fe}/\text{H}] = 0.0$.

Other observations favoured one or the other scenario, which prevented a clear picture of bulge formation to emerge. For example, Zoccali et al. (2008), from the observed sample re-analysed later by Babusiaux et al. (2010), found a clear metallicity gradient in the bulge; this was interpreted as a challenge to the scenario in which the bulge would result solely from the vertical heating of the bar. On the other hand, recent radial velocity studies (Howard et al., 2008, 2009; Shen et al., 2010; Kunder et al., 2012) find that the radial velocity dispersion (σ_{RV}) of bright bulge giants is fully consistent with the pseudo-bulge scenario. In particular, Shen et al. (2010) show that any classical bulge contribution cannot be larger than $\sim 8\%$ of the disc mass. Furthermore, recent spectroscopic studies of the abundances of the α -elements as a function of $[\text{Fe}/\text{H}]$ revealed that at least the metal-poor bulge stars are chemically similar to stars in the local thick disc (Meléndez et al., 2008; Alves-Brito et al., 2010; Ryde et al., 2010) and the inner disc at Galactocentric distances of 4 to 7 kpc (Bensby et al., 2010b).

A comprehensive summary of the current observational picture of the bulge structure, formation, and evolution cannot be given in this paper. Instead, we refer to the recent review by Rich (2011). In any case, it is clear that the current observational evidence is not sufficient to conclusively constrain the structure and formation history of the Galactic bulge, and that more observations are required.

In the past, most of the attention has been paid to the intermediate bulge, e.g. Baade’s window toward $(l, b) = (+1^\circ, -3.9^\circ)$, while the outer bulge has been somewhat neglected. This may explain why an important feature such as the double red clump (RC), which becomes apparent only at $|b| \gtrsim 5^\circ$, was detected only recently (Nataf et al., 2010; McWilliam & Zoccali, 2010). This feature is interpreted as two over-densities of bulge stars at different distances from the sun (McWilliam & Zoccali, 2010; Saito et al., 2011). It is suggested that the over-densities look like a three-dimensional X-structure (McWilliam & Zoccali, 2010). A first spectroscopic study of stars located in the two RCs was performed by de Propris et al. (2011). These authors could not discern any difference in kinematics and metal abundance between the two RCs, which is in agreement with the interpretation that the two RCs represent the same parent population at different distances from the sun. However, these studies were based on optical spectra with relatively low resolution and signal-to-noise ratio (S/N), from which only an abundance index could be measured. An investigation of the double RC at higher spectral resolution and S/N is desirable to foster these conclusions.

In this Paper we present medium-resolution optical spectra of ~ 400 bulge stars towards a field at $(l, b) = (0^\circ, -10^\circ)$, i.e. ~ 1.4 kpc south of the Galactic plane (assuming a bulge distance of 8.0 kpc) in the outer part of the bulge. The spectra were obtained with the FLAMES spectrograph at the VLT in GIRAFFE multi-object mode. Our sample includes stars from the tip of the RGB to stars less luminous than the expected bump in the red giant branch (RGB) luminosity function (RGB bump), hence it also includes the two RCs. This is the first study of the two RCs with medium-resolution, high-S/N spectra. We measure from these spectra radial velocities, general metallicities, and abundances of iron and the α -elements, and combine this information to obtain a clearer picture of the structure of the outer bulge.

Furthermore, we extensively compare our results with predictions by models of the Galaxy and use these models to infer selection biases and the contamination by non-bulge stars. Recently, Robin et al. (2012) presented a model where two populations co-exist in the bulge region: a bar or pseudo-bulge of high metallicity and small scale height, and a “thick bulge” or classical bulge with a higher scale height, lower metallicity, and higher velocity dispersion. This “Besançon model of the Galaxy” (BGM) explains well the apparent gradient in metallicity that is observed along the minor axis, by a variable proportion of the two populations of different scale height. Here, we use our observed sample as a test case for the new version of the BGM.

The paper is structured in the following way: The sample selection and the observations are presented in Sect. 2; the analysis of the data with the help of COMARCS atmospheric models and spectral synthesis techniques, as well as with the Besançon and TRILEGAL models of the Galaxy, is introduced in Sect. 3; Sect. 4 presents and discusses our results on the radial velocities, metallicities, and α -element abundances; in Sect. 5, a comparison of the Galaxy models with 2MASS photometry is done; finally, conclusions are drawn in Sect. 6.

2. Sample and observations

2.1. Target selection, observations, and data reduction

Initially, the sample of stars was selected for the study of the evolution of lithium along the bulge RGB (Lebzelter et al., 2012). For a detailed description of the sample selection and the observations we refer to that paper, here we reproduce only the most important points.

The selection of targets was based on data from the 2MASS catalogue (Skrutskie et al., 2006) in a $25'$ diameter circle towards the direction $(l, b) = (0^\circ, -10^\circ)$, which is the centre of the Palomar-Groningen field #3 (PG3). The sample selection is illustrated in Fig. 1, which shows a colour-magnitude diagram of that circular field. The observed targets (black circles) were chosen to fall close to two isochrones from Girardi et al. (2000): $Z = 0.004$ and age 10×10^9 years, and $Z = 0.019$ (which is Z_\odot on the scale used by Girardi et al., 2000) and age 5×10^9 years. These isochrones were used because they cover well the RGB of the bulge. They are not chosen as to reproduce any of the GB's properties, in particular not its age spread. A distance modulus of $14^m.5$ to the GB was adopted. The chosen targets were allowed to have a $(J - K_s)_0$ colour either bracketed by the isochrones, or $0^m.02$ redder or bluer than them. Dereddening of the photometry was done as described in Lebzelter et al. (2012). We find a mean reddening of $0^m.129$ in the J -band and $0^m.049$ in the K_s -band. Besides the colour criterion, only stars were included that are fainter than $J_0 = 9^m.0$ to exclude AGB stars above the tip of the RGB, and stars brighter than $J_0 = 14^m.5$ to include the RGB bump, which is expected from isochrones at $13^m.8 \leq J_0 \leq 14^m.1$. This region in the CMD will henceforth be referred to as "selection region". Furthermore, all targets were excluded that had fewer than two quality flags 'A' in the 2MASS JHK_s photometry, and targets that had another source within $3''$ that was not fainter by at least $2^m.0$ in the J -band than the target itself. Applying all those criteria yielded 514 targets for the observations.

The targets were observed with the FLAMES spectrograph, mounted to the VLT UT2 at Paranal observatory, Chile, in the GIRAFFE configuration. The grating HR15 centred at 665 nm was used, which gave a spectral resolution of 17 000 for a wavelength coverage from 644 to 682 nm. The observations were obtained in service mode in June 2009. Of the initially proposed sample, 401 spectra had sufficiently high quality to measure their radial velocity (RV, see below).

2.2. Magnitude histograms and the two RCs

Fig. 2 shows histograms of the 2MASS magnitudes of all stars in the selection region (527 stars, dotted line), and of the stars for which the RV could be determined (401 stars, solid line). At intermediate magnitudes ($13^m.0 \leq J_0 \leq 11^m.5$), spectra of only about 40% of the selected targets are available because one fibre configuration for the stars in this brightness range was not observed. The reduced fraction of actually observed stars will be taken into account in the analysis (Sect. 4.1.1).

Also discernible in Figs. 1 and 2 are the two red clumps (RCs) recently identified by Nataf et al. (2010) and McWilliam & Zoccali (2010). These structures were not known to us in the design phase of the programme. Initially, the fainter RC at $J_0 \sim 13^m.9$ was interpreted as to be the RGB bump, and only the brighter one at $J_0 \sim 13^m.2$ as the red clump. Inspecting Fig. 2, we defined membership of stars in the two RCs as follows. Bright RC: $13^m.65 > J > 13^m.05$, $13^m.05 > H > 12^m.40$,

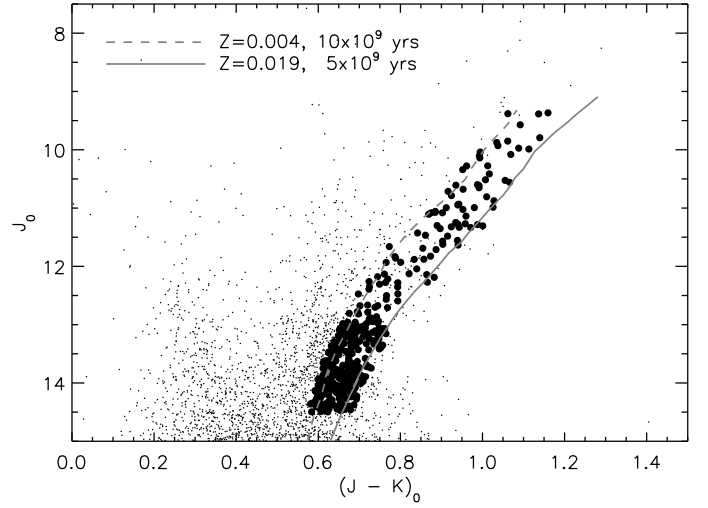


Fig. 1. De-reddened 2MASS colour-magnitude diagram of the $25'$ diameter field around $(l, b) = (0^\circ, -10^\circ)$. Targets observed in the present programme are plotted as black circles, those that have not been observed as black dots. The two RGB isochrones from Girardi et al. (2000) used for the target selection, with ages and metallicities as indicated in the legend, are shown as dashed and solid lines. The isochrones are truncated at the tip of the RGB. The two RCs are the over-densities at $J_0 \sim 13^m.2$ and $J_0 \sim 13^m.9$.

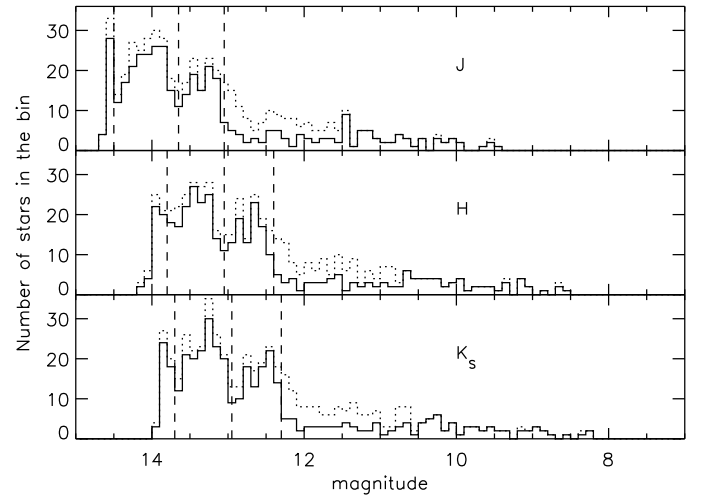


Fig. 2. Histograms of the observed (not de-reddened) 2MASS magnitudes of our sample stars. The dotted line shows the histograms of all stars in the selection region (527 stars, including those that did not fulfil the quality flag criteria to be selected as target), the solid line shows the histogram of the 401 stars for which the radial velocity could be determined. The vertical dashed lines indicate the magnitude limits that were adopted to define the memberships in the two RCs (Sect. 2.2). The double RC is clearly visible in all three bands.

and $12^m.95 > K > 12^m.30$; faint RC: $14^m.50 > J > 13^m.65$, $13^m.80 > H > 13^m.05$, and $13^m.70 > K > 12^m.95$. We found 96 and 150 stars, respectively, which fulfill these criteria. Because it is impossible to ascribe with certainty a given star to either the front or the back arm of the X-structure, the uncertainty of a bulge star's absolute magnitude is about $0^m.35$.

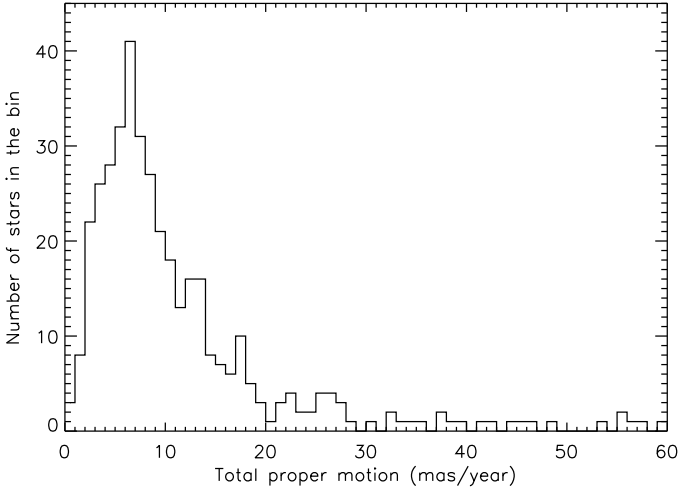


Fig. 3. Histogram of the total proper motion of our sample stars. Stars with a total proper motion larger than 20 mas/year are defined as foreground candidates. Note that four sample stars with a total proper motion larger than 60 mas/year fall outside the plot range.

2.3. Foreground contamination from proper motions

An important issue for this kind of study is the foreground contamination of the sample. The proper motion can be used to identify possible foreground stars. We therefore searched the recently published Southern Proper Motion Program catalogue version 4 (SPM4; Girard et al., 2011) for sample stars with large proper motion. All but ten of our sample stars were found in the SPM4 catalogue. In principle, foreground stars could be identified as those stars whose total space velocity clearly exceeds the maximum measured RV, assuming that they are placed at the distance of the GB (~ 8 kpc). The maximum RV found in our sample is about 300 km s^{-1} , which corresponds to a (tangential) proper motion of 7.91 milli arc-seconds (mas) per year at a distance of 8 kpc. Unfortunately, the mean combined error on the proper motion quoted in SPM4 (6.3 mas/yr) is only barely smaller than this value, so with this catalogue it is impossible to probe in detail the proper motions out to the GB. Applying the criterion described above necessarily would return a mixture of bulge and disc foreground stars. Figure 3 shows the distribution of the total (combined) proper motions of our sample. The distribution essentially consists of a broad peak centred on ~ 7 mas/yr and a long tail of higher proper motion stars. The tail seems to start at ~ 20 mas/yr, which is why we decided to assign those stars to the foreground whose combined proper motion is larger than this value. This is also approximately the number that one gets when two times the mean combined error (2σ) is added to the most common total proper motion. Applying this criterion, we found 50 (12.5%) foreground star candidates, which roughly agrees with the fraction of non-bulge stars estimated from the Galaxy models (see Sect. 3.2.3). The foreground star candidates are marked with an asterisk in Table 3. One star in our sample (#300) has a particularly large proper motion of more than 200 mas/yr, hence it is probably a nearby K dwarf. In addition, #143 is probably a foreground M dwarf.

Unfortunately, there is reason to believe that there are large (systematic) errors in the SPM4 catalogue because the double RC as well as the two peaks in the metallicity distribution (Sect. 4.1.2), two features which are believed to be related to the GB rather than to the disc, are also found among these 50 fore-

Table 1. Parameters of the COMARCS model grid.

$\log g$	J_0 range	T_{eff} (K)
0.6	$9^{\text{m}}0 - 10^{\text{m}}5$	3460, 3625, 3695, 3935
1.1	$10^{\text{m}}5 - 11^{\text{m}}5$	3685, 3830, 4000, 4170
1.6	$11^{\text{m}}5 - 12^{\text{m}}5$	3950, 4140, 4330, 4520
2.1	$12^{\text{m}}5 - 13^{\text{m}}5$	4275, 4450, 4500, 4525, 4725
2.5	$13^{\text{m}}5 - 14^{\text{m}}5$	4425, 4430, 4550, 4645, 4675, 4700, 4750, 4860

ground candidates. Probably there are still many genuine bulge stars among these foreground candidates, which is why we refrain from excluding these stars from the analysis.

3. Analysis

The spectra were analysed with the help of model atmospheres and synthetic spectra, while the results are interpreted with models of the Milky Way galaxy. Both these types of models and the associated analysis are described in the following.

3.1. COMARCS atmosphere models and COMA synthetic spectra

For the analysis of the spectra we used model atmospheres calculated with the COMARCS code (Aringer et al., 2009), and spectra based on these models synthesised with COMA (Copenhagen Opacities for Model Atmospheres; Aringer et al., 2009).

A determination of the stellar temperature and surface gravity with a classical equivalent width analysis using only the FLAMES spectra was not possible due to the relatively small spectral range and the dominance of TiO lines in the cooler targets. Instead, the temperatures of the stars were determined from their 2MASS $(J - K_S)_0$ colour and the effective temperature calibration based on COMARCS models presented in Lebzelter et al. (2012). Hence, the calculations to derive temperatures are consistent with the spectral synthesis applied in this work to obtain abundances in the stars. The surface gravities (g) of the stars were obtained from the J_0 magnitudes of the stars and the isochrones in Fig. 1, assuming that the stars belong to the bulge RGB. The uncertainty in the distance modulus of $\pm 0^{\text{m}}35$ (Sect. 2.2) introduces an uncertainty in $\log g$ of ± 0.16 dex, which however has only a minor impact on the uncertainty in the abundances. Furthermore, a generic micro-turbulence of 2.5 km s^{-1} , typical of red giant stars, a C/O ratio of 0.3, and a generic overabundance of the α -elements (O, Ne, Mg, Si, S, Ar, Ca, and Ti) of $+0.2$ dex were adopted for the model calculations. This overabundance was adopted because previous spectral abundance studies of bulge stars showed a general enhancement of the α -elements of this order of magnitude (e.g. Alves-Brito et al., 2010).

With the temperature, $\log g$, and micro-turbulence fixed in this way, a grid of model atmospheres and associated synthetic spectra was calculated. To keep the grid within reasonable size limits, the RGB was sampled by five different values of $\log g$. For each of these bins, models at various temperatures, in a range applicable for this $\log g$ bin, were calculated. For each combination of $\log g$ and T_{eff} , model atmospheres at five different metallicities $[M/H] = 1.5, -1.0, -0.5, 0.0$, and $+0.5$ were calculated. The parameters of the model grid are summarised in Table 1.

In the next step, spectra were synthesised for all the models in the grid and convolved with a Gaussian to the resolving power

of the observed spectra ($R = \lambda/\Delta\lambda = 17\,000$). The most important line lists used are the one for TiO (Schwenke, 1998), CN (Jørgensen, 1997), and the atomic lines (VALD; Kupka et al., 1999). This last list was checked and improved by comparing a model spectrum of Arcturus (adopting the stellar parameters and abundances found by Ryde et al., 2010) with the observed high-resolution Arcturus spectrum (Hinkle et al., 2000). The solar abundances listed in Caffau et al. (2008) were adopted as reference scale. The solar metallicity on that scale is $Z_{\odot} = 0.0156$.

We emphasise that a particular strength of our method to measure abundances is the consistency of the temperature determination as well as model atmosphere and synthetic spectra calculation, for which the same opacity tables and radiative transfer routines were applied.

3.1.1. Radial velocity measurement

The first quantity that was measured from the spectra was the heliocentric radial velocity. This was done with the help of a cross-correlation technique over the whole available wavelength range, using a synthetic spectrum as template. At this step, a model spectrum with similar temperature as the star under investigation was used for the cross-correlation. The abundance of the model spectrum was not adjusted for each star, we simply adopted solar abundances. The RV was successfully determined for 401 sample stars. We estimated a typical error of $\sim 0.5 \text{ km s}^{-1}$ on the measured RV from a Gaussian fit to the peak in the cross-correlation function.

3.1.2. Determination of the metal abundance

To determine the general metal abundance from the spectra, we employed a simple interpolation and fitting procedure. First, the value for $\log g$ was chosen according to the J_0 magnitude of a given star (see Table 1). Then, all model spectra with that $\log g$ and a given metallicity were interpolated to the temperature of the star using spline polynomials. This interpolation was done for every point of the wavelength vector. For the subsequent fitting procedure, the observed spectrum had to be normalised. For the hotter stars ($T_{\text{eff}} > 3980 \text{ K}$, corresponding to $(J - K_S)_0 < 0.93$) this was done by adjusting the observed flux to the model spectrum flux around a few continuum points. In the spectra of the cooler stars, lines of TiO are appearing or even dominating the spectrum, which prohibit a safe definition of the continuum; therefore, for these stars the observed spectrum was normalised as to have the same median flux as the model spectrum over the used wavelength range. The wavelength range was limited to 649–680 nm (vacuum wavelength). Finally, the metal abundance was determined by a χ^2 minimisation method. The figure of merit to minimise was chosen to be

$$\chi([M/H]) = \frac{1}{N} \sum_{i=1}^N \frac{\sqrt{(f_{\text{obs},i} - f_{\text{model},i}([M/H]))^2}}{f_{\text{obs},i}},$$

where N is the number of wavelength points, and $f_{\text{obs},i}$ and $f_{\text{model},i}$ are the observed and synthetic model flux at wavelength point i . Hence, χ is the mean difference between observed and synthetic model flux, in units of the observed flux. The IDL routine `amoeba.pro` was used to find the metal abundance $[M/H]$ where χ reaches a minimum. The general metal abundance was successfully determined for 383 sample stars.

A few examples of the typically achieved fit qualities are displayed in Fig. 4. This figure shows a zoom-in on the group

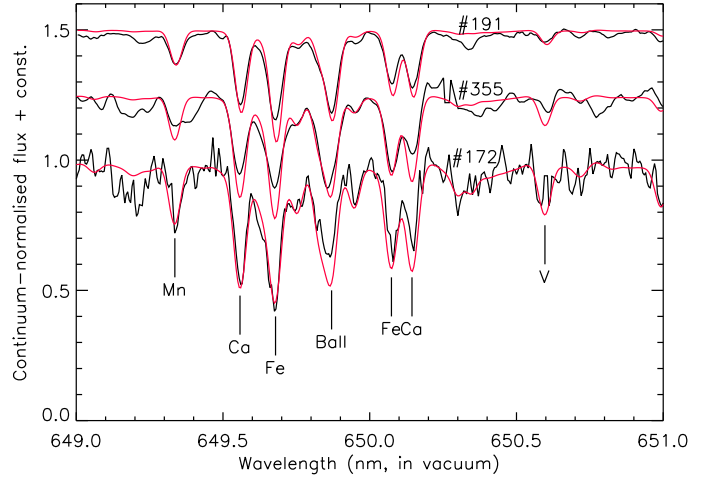


Fig. 4. Typical examples of the fit qualities achieved by our grid interpolation. Observed spectra are plotted as solid black lines, best-fit interpolated model spectra as red lines. From bottom to top: star #172 ($T_{\text{eff}} = 4444 \text{ K}$, $\log g = 2.1$, $[M/H] = +0.06$, $\chi_{\text{min}} = 0.0446$), star #355 ($T_{\text{eff}} = 4547 \text{ K}$, $\log g = 2.5$, $[M/H] = -0.44$, $\chi_{\text{min}} = 0.0303$), and star #191 ($T_{\text{eff}} = 4569 \text{ K}$, $\log g = 2.1$, $[M/H] = -1.05$, $\chi_{\text{min}} = 0.0166$). The spectra of #355 and #191 are shifted vertically by 0.25 and 0.5 for clarity. A few prominent metal lines are identified.

of metal lines located between 649 and 651 nm. An advantage of our fitting method is that it also works well at relatively low S/N because all the information in the whole wavelength range is taken into account. A good example for this is star #172 in Fig. 4.

An illustrative check of our metallicity determination is displayed in Fig. 5, which shows a CMD of our sample stars where the colour of the plotting symbol codes the metallicity of each star. Metal-rich stars tend to be more common at the red edge of the selection region, whereas the metal-poor stars tend to be more abundant on the blue edge. This is what can be expected from the evolution along the RGB: at a given brightness, a metal-rich star will be cooler, hence redder in $(J - K_S)_0$, than a metal-poor star. This suggests that our methods for temperature and metallicity determination work well. Additional sub-structure around the double RC is hidden by the high density of stars in that figure; it will be discussed in more detail in Sect. 4.3.

There are a few sample stars for which the fitting routine extrapolated beyond the abundance range covered by the COMARCS model grid. The ten metal-poor outliers clearly have very weak metal lines, indicating a very low metallicity ($[M/H] \lesssim -1.5$). With such a low metallicity, these stars possibly belong to the halo population. The two metal-rich outliers are found at the bright and cool end of the sample.

3.1.3. Determination of the Fe and α -abundance

An estimate of the abundances of iron and the α -elements can be achieved with a procedure very similar to the one above. The only difference here is the non-uniform weighting in wavelength. Weight is put only to those wavelength points that are influenced by line absorption by an α -element or Fe, respectively. Hence, the χ value to minimise was altered to

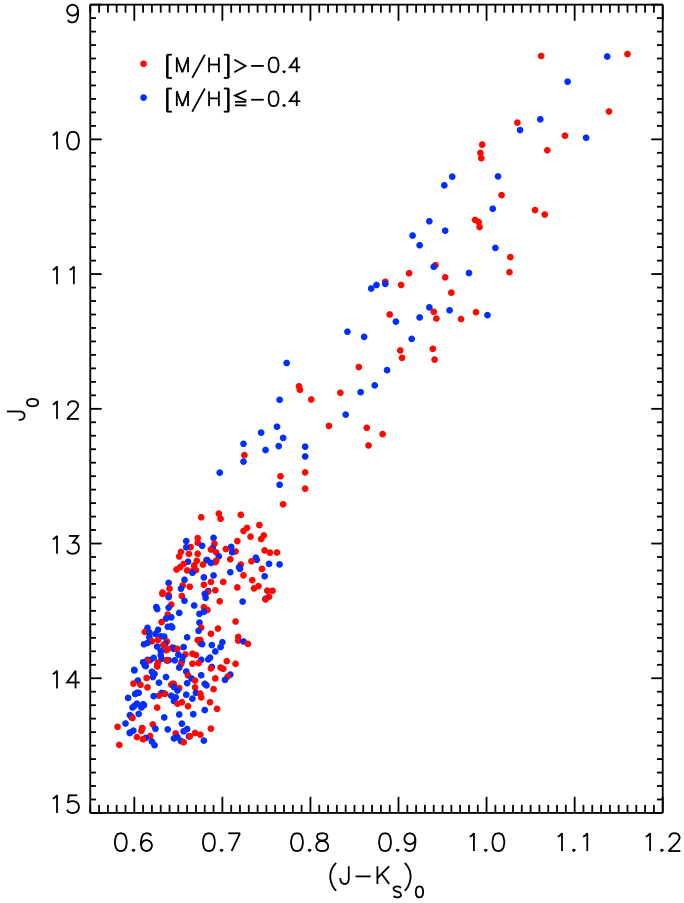


Fig. 5. Colour-magnitude diagram of our sample stars, with the metallicity colour-coded as indicated in the legend. The sample was divided at $[M/H] = -0.4$ into two approximately equally large parts. In particular on the upper RGB, metal-rich stars are preferentially located at the red edge of the selection region, whereas metal-poor stars are preferentially at the blue edge.

$$\chi([\alpha, Fe/H]) = \frac{1}{N} \sum_{i=1}^N W_i \frac{\sqrt{(f_{\text{obs},i} - f_{\text{model},i}([\alpha, Fe/H]))^2}}{f_{\text{obs},i}},$$

where W_i is the weight function. It is a binary function with value 1 for wavelength points with absorption by Fe or an α -element of more than 2% of the continuum flux, and 0 otherwise. The weight function was calculated from a synthetic spectrum based on the model atmosphere with $T_{\text{eff}} = 4450$ K, $\log g = 2.1$, and $[M/H] = -0.50$, taking into account only the α -elements (O, Ne, Mg, Si, S, Ar, Ca, and Ti) or Fe, respectively. The different α -elements will not contribute equally to this mean abundance. In particular, O, Ne, and Ar have no noteworthy lines in our wavelength range. For the other elements, the relative weight on the average α -abundance is: Ca : Ti : Si : Mg : S = 1.000 : 0.751 : 0.400 : 0.027 : 0.009. Hence, the α -abundance is dominated by the individual abundances of Ca, Ti, and Si. The interpolation was done between the grid points at $[\alpha/H] = (-1.3, -0.8, -0.3, +0.2, +0.7)$ and $[Fe/H] = (-1.5, -1.0, -0.5, 0.0, +0.5)$, respectively. The fitting routine did not converge for all stars. Eventually, α -abundances were determined for 368 stars, and Fe abundances for 363 stars. The determination of the iron and α -abundance failed in particular for many of the cool, TiO-dominated stars. The Fe abun-

dance is a very good tracer of the general metal abundance: the mean of $[M/H] - [Fe/H]$ is -0.13 dex, with a standard deviation of 0.12 dex; the standard deviation decreases to only 0.07 dex among the sample stars fainter than $J_0 = 12^m$.

All measured abundances and radial velocities can be found in Table 3 in the on-line Appendix.

3.1.4. Systematic errors

A check of our relatively simple methods for the metallicity and abundance determination was done by applying it to the spectrum of Arcturus. For this star, our method yields a metallicity of $[M/H] = -0.72$, and $[Fe/H] = -0.92$. If dedicated model atmospheres with the parameters from Ryde et al. (2010) are used ($T_{\text{eff}} = 4280$ K, $\log g = 1.7$), i.e. if the grid interpolation in temperature is avoided, $[M/H]$ increases to -0.69 . Models without an α -enhancement (i.e. scaled solar abundances) yield $[M/H] = -0.64$. A search on the Simbad database¹ shows that most studies find $[Fe/H] \sim -0.50$ for Arcturus.

To back-up the existence of a systematic abundance offset, we made a blind test with four stars from the sample of Gonzalez et al. (2011a), which cover a range of almost 1 dex in $[Fe/H]$. The spectra of the stars in the FLAMES HR15 setting were kindly provided by O. Gonzalez (private communication) and their stellar parameters as determined in Zoccali et al. (2008) were communicated, but not their individual abundances. The same fitting routine as for our sample stars were applied to the spectra. The results were then compared to those of Gonzalez et al. (2011a). The Fe abundances derived with our method were systematically lower by 0.19 to 0.29 dex than those of Gonzalez et al. (2011a).

Systematic abundance offsets of 0.2 to 0.3 dex between equivalent width measurements and χ^2 minimisation techniques (in the sense that the χ^2 minimisation gives lower abundances) have also been reported by the RAVE survey team (Zwitter et al., 2008; Boeche et al., 2011), in particular for giant stars. No explanation as for the possible origin of this offset is given in the literature, neither did we attempt to track down its cause. One explanation could be that the classical equivalent width measurement uses only relatively few lines, selected to be unblended, whereas the χ^2 minimisation uses many more lines, even blended and partially saturated ones. While the reasons are only speculative at this point, we decided to add 0.2 dex to all abundances determined here. This does not only yield better agreement with the comparison stars of Gonzalez et al. (2011a) and Arcturus, but, as we will see below, gives very satisfactory agreement with other studies of abundances in GB stars. The thereby *corrected abundances* will be used henceforth in the analysis of our data set and are also reported in Table 3. Despite the systematics in the abundance scale, we are nevertheless confident that our abundance determination is reliable in the relative sense within the sample. Furthermore, we decided to base our analysis mainly on the $[M/H]$ measurement because it is available for a few more stars, in particular more of the bright stars. The results would remain qualitatively unchanged if $[Fe/H]$ was used instead.

3.1.5. Uncertainty estimate

The uncertainty in the determination of the metallicity was estimated for six representative sample stars covering a range in temperature, metallicity, brightness, and S/N ratio. This was done mainly by varying the free parameters within their uncertainties, one at a time while keeping the others constant, and then

¹ <http://simbad.u-strasbg.fr>

repeating the fitting process. Uncertainties arising from the determination of temperature and $\log g$, as well as in the continuum placement, were taken into account.

The uncertainty in the effective temperature was determined from the uncertainty on $(J - K_S)_0$ by adopting the uncertainties in the J - and K_S -band magnitudes given in the 2MASS catalogue. For the bright (cool) stars this uncertainty is between 60 and 100 K, while for the faint (hot) ones it is between 130 and 200 K. However, this does not mean that the temperature has a lower impact on the $[M/H]$ determination for the bright and cool stars, just on the contrary: because their spectra are dominated by the very temperature-sensitive TiO bands, a change in temperature has the largest impact on their metallicity determination. Uncertainties up to 0.27 dex from the temperature uncertainty alone were found, but for most stars it is in the range 0.09 to 0.18 dex.

The uncertainty coming from the $\log g$ estimate was determined by doing the interpolation and fitting with a group of model spectra adjacent in $\log g$ to the one that would be attributed to a given star based on its J_0 magnitude. We found that the $\log g$ estimate contributes 0.06 – 0.10 dex of uncertainty in the $[M/H]$ determination. This should already include the uncertainty coming from the fact that we interpolate model spectra to the temperature of the stars, rather than using model spectra calculated for the exact temperature of every star.

Finally, the uncertainty introduced by the continuum placement was estimated by varying the normalisation factor within its uncertainty range, derived from the scatter of the pixels in the continuum points. This uncertainty mainly depends on the S/N of the spectrum, and contributes another 0.02 – 0.04 dex to the uncertainty in $[M/H]$. Thus, for most stars the combined uncertainty in $[M/H]$ is in the range 0.11 – 0.21 dex, but it can be as high as 0.30 dex for the cool stars dominated by TiO absorption. The uncertainties in the iron and α -element abundances are very similar.

3.2. The Besançon and TRILEGAL models of the Galaxy

3.2.1. The Besançon model

The Besançon Galaxy Model (BGM) is based on assumptions on the scenario of formation and evolution of four main stellar populations of the Milky Way (Robin et al., 2003). It allows to simulate the stellar content in any given line of sight, and for each simulated star the photometry, kinematics, and metallicity are computed. For each population, the main assumptions are: a star formation-rate history, age, and initial mass function, which allow to generate a distribution function in absolute magnitude, effective temperature, and age of the stars. These assumptions are confined by observations, such as the stellar content in the solar neighbourhood, remote star counts, and photometry in the visible and near-infrared. Density laws are assumed and controlled by dynamical principles (Bienaymé et al., 1987) for each population and are tested by means of photometric star counts. The model has been extensively compared with 2MASS data which allow to constrain the thin disc parameters quite well, such as the scale length, scale height, the inner disc hole, and the warp (Reylé et al., 2009). However, some model parameters are not well constrained yet, such as for the thick disc population. When a parameter is not yet well constrained from available data, such as metallicity gradients for example, a mean value from the literature is assumed, or a value expected from standard scenario of formation. For example, thick disc parameters are still controversial: its density parameters such as the local density and

the scale height are degenerated when obtained by model fitting from high galactic latitude fields (Robin et al., 2012). However, in the direction considered here, the thick disc population remains marginal. We conservatively use here the thick disc parameters determined from high latitude counts by Reylé & Robin (2001).

Once density functions and distribution functions are obtained, the simulated stars are generated in the whole Galaxy divided in volume elements. A number of improvements have been made to the model since the one presented in Robin et al. (2003). The mean metallicity and dispersion about the mean for each age bin in the thin disc are now taken from Haywood (2008), rather than from Twarog (1980). The model also includes a 3D extinction map (Marshall et al., 2006) and photometric errors are added for comparison with observations.

Recently, a new model of the bulge/bar region has been proposed by Robin et al. (2012), which we will use here to interpret and compare to our observed data. The new model includes a bar and a “thick bulge”. In the following, this latter population will be referred to as the *bulge* when discussing the BGM. The bar is the most massive component, which dominates the stellar content at low latitudes. The bulge is longer and thicker and gives a contribution at intermediate latitudes where the bar starts to be less prominent. The main bar population has a mean metallicity close to solar, while the bulge population is found to be more metal-poor, with a metallicity of the order of -0.4 to -0.5 dex. The mean metallicities and dispersions of these two populations have been roughly estimated from the observed MDF by Zoccali et al. (2008). It should be better constrained in the future using larger samples and more lines of sights in the inner and outer bulge.

A large hole in the central region causes the thin disc to reach its maximum density at about 2.5 kpc from the Galactic centre. The kinematics of the thin disc follow empirical estimates from Hipparcos (Gomez et al., 1997), while for the thick disc it is taken from proper motion data from Ojha et al. (1996), and for the halo from Norris et al. (1985), as in Robin et al. (2003). In the version presented here, the bar kinematics are taken from the dynamical model of Fux (1999). The bulge is found to have a larger velocity dispersion, close to the one of the halo (Robin et al., in preparation).

The fact that the bar population has a smaller velocity dispersion, a higher metallicity, and a smaller scale height than the bulge allows to explain well the vertical gradient of metallicity seen in bulge fields along the minor axis (Zoccali et al., 2008). Babusiaux et al. (2010) already suggested that the origin of the metallicity gradient could be a varying mix of these two populations. The bar and bulge populations in the BGM do not have an intrinsic metallicity gradient. This model also explains well the presence of double clumps at medium latitudes, as seen in Nataf et al. (2010), McWilliam & Zoccali (2010), and Saito et al. (2011). This derives from the fact that the bar flares from inside to outside by about 30%. This flare can be due to resonances in the bar that trap thin disc stars and scatter them to higher scale height.

3.2.2. The TRILEGAL model

The TRILEGAL model was developed by Girardi et al. (2005) and is a population synthesis code for simulating the stellar photometry of any field in the Milky Way galaxy. The model has proven to well reproduce number counts, amongst others, in all three pass-bands of the 2MASS catalogue, with errors smaller than ~ 30 per cent (Girardi et al., 2005). The bulge component

was introduced in TRILEGAL only later by Vanhollebeke et al. (2009), who also calibrated its stellar population and metallicity distribution using photometry from the 2MASS and OGLE-II surveys of red clump stars. The input MDF for the bulge component in TRILEGAL was obtained by Vanhollebeke et al. (2009) with the help of a fitting procedure to the RC star distribution, by applying shifts to the photometric MDF of Zoccali et al. (2003). The best fit was obtained with a shift of +0.3 dex. Note that Vanhollebeke et al. (2009) used fields that are considerably closer to the Galactic plane than our field, at most 5.91° south of the plane.

Their best-fit bulge model is provided as the default in the interactive web interface to TRILEGAL², which we also used here to simulate the stellar content of our FLAMES field. Other important ingredients that we adopted included: a binary fraction of 0.3 with mass ratios between 0.7 and 1.0; an exponential extinction law with an extinction value at infinity equal to the one used to deredden the observed photometry ($0^m.526$ in the V -band); a thin and a thick disc, both with squared hyperbolic secant density distributions; and a halo with an oblate $r^{1/4}$ spheroid density distribution. For all these components, the default parameters offered on the web interface were adopted. The TRILEGAL model does not provide for the kinematics of its simulated stars, hence a comparison with our observations was not possible in this respect.

A circular field of $25'$ diameter centred on the point $(l, b) = (0^\circ, -10^\circ)$, equal to the area from which the observed targets were selected, was simulated with both models. An exception here is that for the BGM we also calculated ten simulations with identical parameters, to decrease the Poisson noise mainly for the comparison with the observed RVs. For all subsequent comparisons between spectroscopic observations and the Galaxy models, the same photometric selection criteria were applied to the models as to the observed sample (Sect. 2.1). In Sections 4 and 5, we will confront the model predictions with our observations in terms of kinematics, abundances, and photometric properties.

3.2.3. Inferring metallicity biases, foreground contamination, and mass distribution with the Galaxy models

The Galaxy models can be very useful to infer a number of important properties of the observed sample, in particular metallicity biases imposed by our photometric selection criteria, (foreground) contamination by non-bulge stars, and the distribution of initial masses.

The location of a bulge star in a CMD, and hence its probability to fall in our selection region, is determined by a complex interplay of metallicity, distance, age, reddening, and photometric errors. The ratio of the input MDF for the bulge (and bar) component to the MDF of the stars selected with our procedure reveals any such metallicity biases. An inspection of this ratio for the BGM simulation shows that there exists a small bias against intermediate metallicities ($[M/H] \sim -0.4$). This is probably caused by the different distance distributions of the bulge and the bar component in the BGM: the bulge component, which contributes most stars in this intermediate to low metallicity, is spread out between 2 and 14 kpc distance from the sun, whereas the bar, which is centred around solar metallicity, is much more concentrated around 7 kpc distance. Many of the nearby bulge stars thus do not fall in the selection region, which causes this small bias against intermediate metallicity stars. In fact, an in-

spection of the distance distribution shows that our selection procedure is relatively efficient in picking up stars at distances between 5 and 11 kpc.

The TRILEGAL model includes a single bulge component, with a distance distribution centred on 7 kpc. Hence, the metallicity bias inferred from this model somewhat differs from the one found from the Besançon model. The ratio of input MDF to the MDF in the selection region is relatively flat in a broad range from $[M/H] \sim -0.4$ to $+0.5$, but gradually decreases to lower metallicities. This is also what one would expect from a bulge population with a relatively small distance spread: because low-metallicity stars evolve along the RGB at relatively blue $J - K_S$ colours, in particular on the upper RGB, they would be missed by our selection procedure (along relatively metal-rich isochrones) with a higher probability. Consistent with this expectation, we find in both models that the metal-poor stars in the selection region are preferentially at larger distances than the metal-rich ones because the blue, metal-poor stars are shifted into the selection region when they are at large distances.

Both the Besançon and TRILEGAL model allow to assign a simulated star to one of the stellar components of the Milky Way, by which means we estimated the fraction of genuine bulge stars in our sample. The selection of stars from the Besançon model yielded 688 stars, of which 333 (48.4%) belong to the thick bulge, 216 (31.4%) to the bar (hence 79.8% of bulge/bar stars in total), 72 (10.5%) to the thin disc, 64 (9.3%) to the thick disc, and 3 (0.4%) to the halo. On the other hand, in the TRILEGAL model 509 stars fall in the selection region, of which 479 (94.1%) belong to the bulge, 21 (4.1%) to the thin disc, 9 (1.8%) to the halo, and none to the thick disc. From this estimate we conclude that a large fraction ($\geq 80\%$) of our sample stars are genuine bulge stars. Most of the foreground contamination comes from the thin disc, while the halo contamination should be very small. The fraction of non-bulge stars agrees reasonably well with the fraction of foreground star candidates selected on basis of their proper motion (12.5%) in Sect. 2.3. Most notably, applying the same proper motion selection criterion of > 20 mas/yr to the simulated stars in the Besançon model retrieves 52 foreground star candidates, in excellent agreement with the number we found from the SPM4 catalogue. Of these 52 stars, 51 are thin disc stars and one is a thick disc star.

The distribution of initial masses of the simulated stars turns out to be relatively sharply peaked in both models. In the Besançon model the mean mass is $1.05 M_\odot$ with a standard deviation of $0.11 M_\odot$, whereas in TRILEGAL the mean is at $1.13 M_\odot$ with a standard deviation of $0.14 M_\odot$. Genuine bulge stars have an even narrower distribution: $1.07 \pm 0.05 M_\odot$ in the Besançon model and $1.15 \pm 0.09 M_\odot$ in the TRILEGAL model. The most massive stars selected from the simulated data have 1.39 and $1.59 M_\odot$ in the Besançon and TRILEGAL model, respectively. Hence, we are confident that our sample contains mostly low-mass ($M \sim 1.1 M_\odot$) red giant stars located in the GB.

4. Results and Discussion

4.1. The observed metallicity distribution function

4.1.1. Whole sample

The MDF of our sample stars is displayed in Fig. 6. Two versions are plotted: The raw MDF (solid line), and a MDF corrected for the incompleteness in some brightness (and hence colour) ranges in our sample. To correct for this, we applied a bootstrapping method similar to method ii) used by Zoccali

² <http://stev.oapd.inaf.it/trilegal>

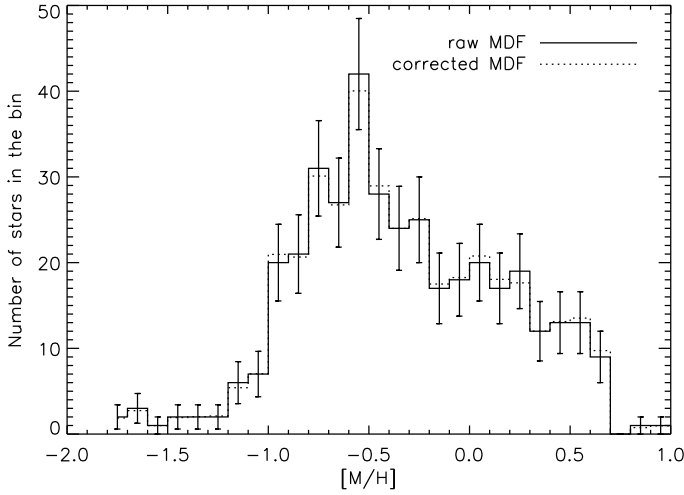


Fig. 6. Metallicity distribution function of all 383 sample stars with determined metallicities. The solid line is the raw MDF, while the dotted line is an MDF corrected for the non-uniform fraction of observed vs. available targets as a function of magnitude, using a bootstrapping method. Poissonian noise error bars are also shown for the raw MDF.

et al. (2008). In this method, stars are drawn randomly until a flat ratio of observed to available stars is reached. Zoccali et al. (2008) considered this ratio as a function of colour. Instead, we chose to consider it as a function of brightness because our targets were grouped for observations according to their brightness, where one of the scheduled settings for the intermediate brightness group was not observed. However, since our selection region diagonally crosses the CMD, any under-sampling in colour bins will be effectively corrected for by this method. Two-hundred such randomly drawn MDFs were created and averaged, the result of this procedure is plotted as dotted line in Fig. 6. The corrected MDF is only marginally different from the raw MDF, hence we conclude that our sample well represents the metallicities of stars in the whole selection region.

The MDF is broad with a clear peak at $[M/H] \sim -0.55$. The median, mean³, and standard deviation of the MDF are -0.41 , -0.34 , and 0.51 dex. This mean metallicity agrees well with what Zoccali et al. (2008) found: for fields at $b = -6^\circ$ and $b = -12^\circ$ they found $\langle [Fe/H] \rangle = -0.21$ and -0.29 , respectively. Interpolating between these fields to $b = -10^\circ$ yields a mean of -0.26 . Note, however, that Zoccali et al. (2008) estimated a large contamination by thin and thick disc stars in their sample at $b = -12^\circ$, which may have a considerable impact on the mean metallicity of this field. Whereas Zoccali et al. (2008) used a box in an I vs. $V - I$ colour-magnitude diagram to select their targets, we used a selection region along isochrones, a strategy that is probably much more discriminant against thin and thick disc contaminants. Johnson C. et al. (2011) derived spectroscopic iron abundances of RGB and RC stars in two fields at $(l, b) = (0^\circ, -8^\circ)$ and $(l, b) = (-1^\circ, -8.5^\circ)$. The mean $[Fe/H]$ found for these fields are -0.34 and -0.27 , respectively. These authors also derive photometric metallicities for the latter field and find a median of $[Fe/H] = -0.34$. Also Gonzalez et al. (2011b) derived photometric metallicities along the GB minor axis and find $\langle [Fe/H] \rangle = -0.36$ in a $30' \times 30'$ field around

³ Doing the averaging on a *linear* scale, which is the mathematically correct way, the mean is $[M/H] = -0.05$, converted back to the logarithmic scale.

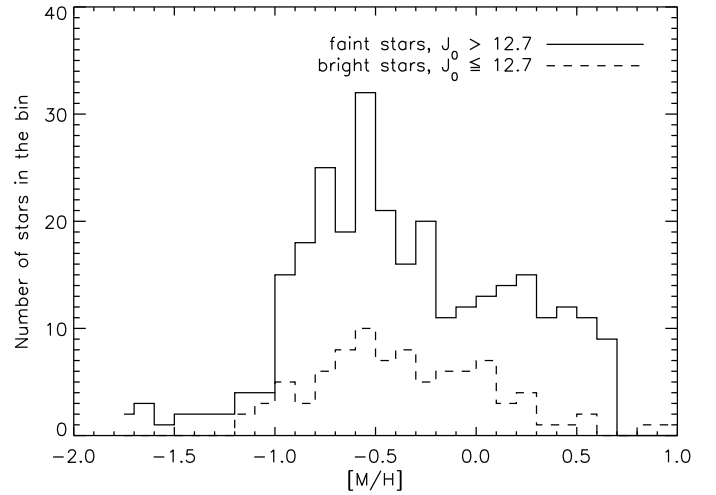


Fig. 7. Metallicity distributions of bright ($J_0 \leq 12^m.7$, dashed line) and faint ($J_0 > 12^m.7$, solid line) sample stars. The metal-poor and metal-rich populations are more clearly separated among the faint sample stars.

$b = -8^\circ$. These values all agree nicely with one another, and with our result for the field at $b = -10^\circ$.

The MDF in Fig. 6 exhibits a relatively sharp cut-off at $[M/H] \sim -1.0$. This could be related to the use of an isochrone with $Z = 0.004$ (corresponding to $[M/H] = -0.68$) for defining the blue edge of the selection region. As suggested by the TRILEGAL model (Sect. 3.2.3), there probably is a bias against metal-poor stars in the selection, which affects the size and shape of the metal-poor peak. This metallicity selection bias will be smoothed by the distance spread of the bulge stars. However, it is hard to quantify if this sharp cut-off is a real feature or an effect of the selection bias because of the lack of stars with $[M/H] \lesssim -1.0$ in the input MDF of the models.

4.1.2. Bright and faint sample stars

It becomes clear already from Fig. 6 that there are possibly two peaks in the MDF: one at ~ -0.55 and one at ~ 0.2 . This double-peak structure becomes even more apparent if bright and faint stars are considered separately (Fig. 7). The cut between bright and faint stars was introduced at $J_0 = 12^m.7$, which should safely exclude RC stars from the bright sub-sample. The motivation to introduce a brightness cut is two-fold: first, the uncertainty in the metallicity is larger (~ 0.30 dex) for the coolest and brightest sample stars. Thus, with a brightness cut we exclude stars with the most uncertain metallicity determination. Second, a brightness cut is equivalent to a cut in evolutionary state, at least when the distance spread within the bulge of $\sim 0^m.7$ is disregarded. Hence, with our sample we can check whether the MDF varies with evolutionary state or not.

The most striking feature in Fig. 7 is that among the faint sample stars (those with $J_0 > 12^m.7$) the dichotomy in metallicities becomes even clearer than in the complete sample. To make this dichotomy more quantitative we performed a decomposition by Gaussian mixture models. The parameter space of two Gaussian mixture models was explored using a Markov Chain Monte Carlo simulation and a maximum-likelihood approach to define the best-fit parameters (for details on the code see Nataf et al. (2011), for an in-depth explanation of MCMCs see Johnson J. A. et al. (2011)). The chosen confidence level is 68%. Stars with $[M/H] < -1.4$ were omitted from the fit because

we think these stars might be halo contaminants. The results of this Gaussian decomposition are presented in Fig. 8. We find mean metallicities of the populations of $[M/H] = -0.57 \pm 0.03$ and $[M/H] = +0.30 \pm 0.04$, and dispersions of 0.27 ± 0.02 and 0.28 ± 0.03 dex for the metal-poor and metal-rich population, respectively. The metallicity difference between the two populations, the systematically and statistically more robust figure, is $\Delta[M/H] = 0.87 \pm 0.03$. The number of stars belonging to those peaks is 198 ± 12 and 88 ± 12 , respectively, yielding a fraction of the metal-rich population of $(30.8 \pm 4.2)\%$. The TRILEGAL model suggests that there could be a selection bias against metal-poor stars (Sect. 3.2.3); if true, then the fraction of metal-poor stars at this Galactic latitude has to be regarded as a lower limit, and that of the metal-rich ones as an upper limit.

4.1.3. Comparison with the literature

Recently, MDFs of bulge stars were presented by Hill et al. (2011) and Bensby et al. (2011), both of which find a double-peaked MDF. Hill et al. (2011) presented $[Fe/H]$ measurements for 219 bulge red clump stars in Baade’s window ($b = -4^\circ$), derived also from FLAMES/GIRAFFE spectra. Their Gaussian decomposition yields a broader peak at $[Fe/H] \approx -0.30$ and a relatively narrow peak at $[Fe/H] \approx +0.32$, respectively. On the other hand, Bensby et al. (2011) measured from high-resolution UVES/VLT spectra the metallicities of micro-lensed dwarf and sub-giant stars scattered throughout the Galactic bulge at latitudes between $b = -1^\circ$ and -5° , at various longitudes. The dwarfs show also a clearly bi-modal distribution with peaks at $[Fe/H] \approx -0.60$ and $\approx +0.3$. Our result is in excellent agreement with that of Bensby et al. (2011), even though our field is several degrees (corresponding to ~ 1 kpc) away from the dwarfs analysed by these authors. Only the metal-poor population identified by Hill et al. (2011) has a higher metallicity by ~ 0.3 dex. Unfortunately, the number of analysed bulge dwarfs is still too low to reliably estimate the widths of the two peaks in their MDF. In contrast to the results of Hill et al. (2011), the peaks in the MDF found in our sample have very similar widths. In general, there are interesting analogies between our results and those of Bensby et al. (2011) and Hill et al. (2011), and we conclude that there are two populations present in the GB, separated by $0.6 - 0.9$ dex in metallicity. The small differences might be a result of the different selection procedures, the difference in evolutionary state of the samples, and the different analysis methods applied in the studies.

4.2. Evolutionary effects on the MDF

Another interesting feature of Fig. 7 is the probable lack of metal-rich stars among the bright sample stars ($J_0 \leq 12^m7$). In the metallicity range $+0.1 \leq [M/H] \leq +0.7$, eleven stars are bright and 72 stars are faint ($13.3 \pm 4.3\%$ bright stars, the uncertainty being calculated from Poissonian noise), whereas in the range $-0.5 \leq [M/H] \leq +0.1$ the fraction is $29.5 \pm 5.4\%$ (39 bright and 93 faint stars). The fraction of bright stars in the whole sample is $22.9 \pm 2.7\%$ (92 bright and 309 faint stars). This reduced fraction of bright stars among the metal-rich stars could be caused by a selection effect. We therefore inspected the fraction of bright stars in the selection region of the Galaxy models as a function of metallicity to check for differences in the metallicity bias between faint and bright RGB stars (i.e. less and more evolved stars). However, no such trend is found, which suggests that the metallicity biases equally apply to faint and bright stars.

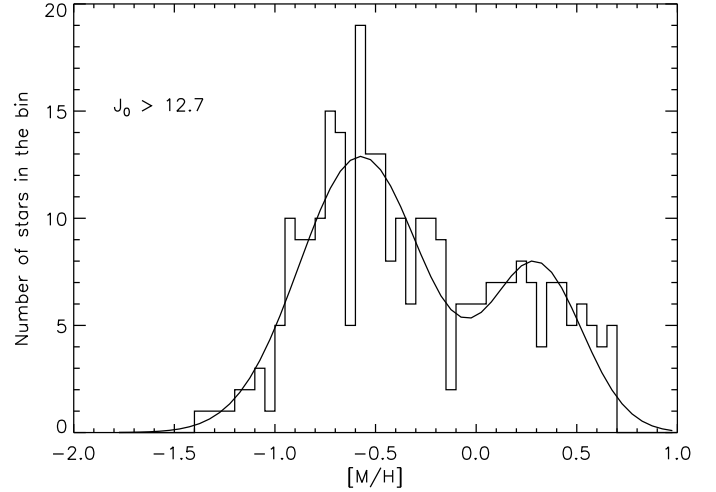


Fig. 8. Metallicity distribution of the faint sample stars ($J_0 > 12^m7$) together with the two best-fitting Gaussian mixture models. The metallicity distribution in this brightness range is clearly bimodal.

Apparently, the shape of the MDF depends on the evolutionary state of the sample stars one is considering. The simplest explanation for this finding is that the metal-rich stars do not evolve all the way from the main sequence up to the RGB tip or the early AGB, but get “lost” somewhere on the way (e.g. due to enhanced mass loss; Castellani & Castellani, 1993). A similar scenario was put forward by Chiappini et al. (2009) to explain the shift of 0.3 dex to lower values in the planetary nebulae oxygen abundance distribution with respect to the distribution of giant stars. Because of the still relatively small number of stars in the present sample this conclusion has to be taken with some caution. Also, some (presumably metal-rich) stars on the red side of the selection region have not been observed in the present programme (see Fig. 1). However, in Sect. 4.7.3 we will present another piece of evidence from the radial velocity dispersion of evolved stars that strongly supports the scenario of metallicity-dependent mass loss.

4.3. The metallicity of the red clump stars: Is the double RC only connected to the metal-rich population?

Figure 9 shows the MDF of the bright and faint RC, with the definition of the two RCs as introduced in Sect. 2.2. It is clear from that figure that the faint RC has a much more prominent low-metallicity peak than the bright RC, which in turn shows both peaks. Their mean metallicities are $[M/H] = -0.18$ and -0.41 , respectively. This would suggest that the two RCs have intrinsically different metallicities, in contradiction to findings by de Propris et al. (2011), and would therefore not represent the same underlying population of stars. However, we believe that this seemingly different mean metallicity is actually caused by our selection procedure. Because of the way how we selected the stars along two isochrones, which become redder at brighter magnitudes, there are preferentially redder stars selected from the bright RC, and bluer stars from the faint RC (see also Fig. 5). At a given evolutionary state, redder stars are more metal-rich than bluer ones. Hence, we selected preferentially more metal-rich stars in the bright RC than in the faint RC. This interpretation is also favoured by the RV distributions of the two RCs, which are practically indistinguishable (cf. Sect. 4.6). Introducing an additional colour criterion does not strengthen

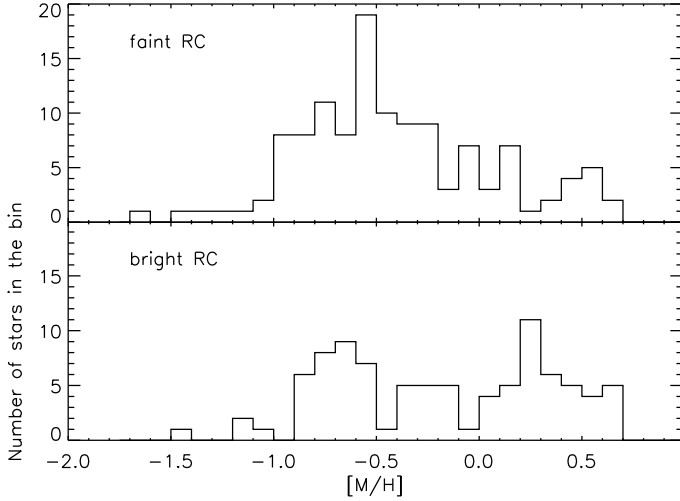


Fig. 9. Metallicity distribution of stars belonging to the faint (*upper panel*) and bright (*lower panel*) RCs, respectively.

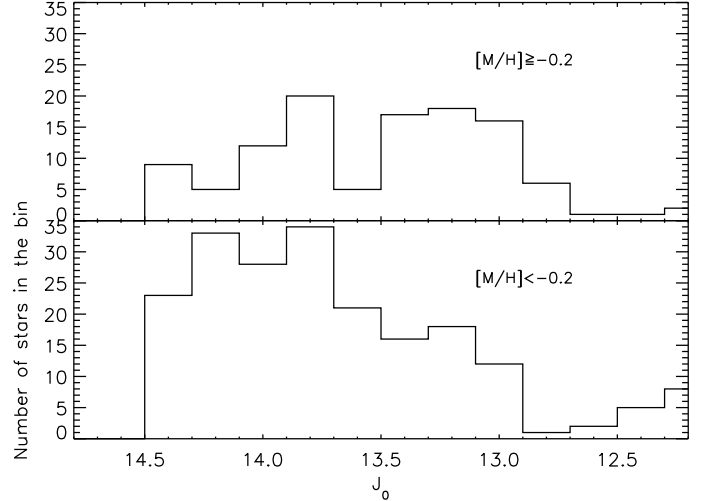


Fig. 10. Luminosity functions of the metal-rich ($[M/H] \geq -0.2$, *upper panel*) and the metal-poor ($[M/H] < -0.2$, *lower panel*) populations around the red clump brightness.

this conclusion because of the small number of stars that would be compared then.

In fact, we suggest that the double RC feature is connected only to the metal-rich population. A direct hint may come from the luminosity functions of the metal-poor and metal-rich populations around the RC brightness, see Fig. 10. The metallicity cut was introduced at $[M/H] = -0.2$ for this diagram. The metal-rich population has two peaks in the J_0 histogram, one at $J_0 \sim 13^m2$ and one at $J_0 \sim 13^m9$. It stands to reason that these two peaks are the manifestation of the front and back arms of the X-shaped bulge. The fainter peak contains fewer stars because its stars are at larger distance from the Galactic plane where the density of stars is lower (Saito et al., 2011). The metal-poor population has one very broad, symmetric peak at $J_0 \sim 14^m0$ with a decline towards brighter magnitudes. Because the RC and the RGB bump have the same magnitude in J_0 at a metallicity of $[M/H] \approx -0.7$ (Nataf et al., 2011), this peak may also contain some RGB bump stars of the metal-poor population. A statistical t-test shows that the probability that the two luminosity functions are drawn from the same parent distribution is only 5.1%. Also Ness et al. (2012), from an analysis of spectra of clump stars along the minor bulge axis, find that a split in the luminosity function appears only for stars with $[Fe/H] > -0.5$, in good agreement with our finding.

Another argument for the suggestion that the double RC feature is connected only to the metal-rich population may come from the analogy of how the double RC feature diminishes with increasing distance from the Galactic plane and the presence of a metallicity gradient in the bulge. CMDs based on 2MASS photometry in three different fields along the minor axis of the bulge (at $b = -7.0^\circ$, -8.5° , and -10.0° , from top to bottom) are shown in Fig. 11. Fields with radii of $20'$, $30'$, and $40'$, respectively, were used to keep the total number of stars approximately constant. On the right hand side of each panel, a magnitude histogram of the stars inside the box marked by thick lines is shown. The luminosity function was fitted with Gaussian and exponential functions to reproduce the RCs, RGB bump, and the underlying distribution of RGB stars. It is clear from that figure that not only the peak brightness positions of the RCs are moving apart when going away from the plane, but also the relative number of stars making up the double RC feature is decreasing with distance from the plane.

Together with the presence of a metallicity gradient in the bulge (Zoccali et al., 2008), this suggests that the double RC feature is connected only to the metal-rich population, which is much more concentrated towards the Galactic plane. In both Hill et al. (2011) and Bensby et al. (2011) the stars evenly distribute among the two sub-populations. In our sample, the metal-rich population makes up only $\sim 30\%$ of the stars (upper limit), which would suggest that the fraction of the populations varies with Galactic latitude. Hence, the metal-rich population seems to be more concentrated towards the plane than the metal-poor one. This would also explain the metallicity gradient found by Zoccali et al. (2008): If the fraction of metal-rich stars decreases with increasing distance from the plane, also the mean metallicity would shift to lower values. Hence, rather than a decreasing mean metallicity within one monolithic bulge population, probably it is the varying percentage of two sub-populations that *mimics* a metallicity gradient in the bulge.

4.4. Comparison with simulated MDFs

Our observed MDF, corrected for sampling effects (Sect. 4.1.1), is compared to the simulated MDFs from the Besançon and TRILEGAL models in Fig. 12. The simulated MDFs do not reproduce the observed MDF in all aspects. The MDF of the TRILEGAL model has clearly a much higher mean metallicity than the observed mean ($[M/H] = +0.09$, compared to -0.34). The number of metal-poor stars is underestimated, whereas the super-solar metallicity stars are overrepresented in the TRILEGAL model. Clearly, the shift of $+0.3$ dex applied by Vanhollebeke et al. (2009) to the MDF of Zoccali et al. (2003) does not reproduce the MDF of our sample (which is at -10° from the Galactic plane). This probably means that an MDF calibrated on fields at low Galactic latitude cannot be simply applied to higher latitudes because of the metallicity gradient. The mean metallicity in the Besançon model, on the other hand, is close to the observed one ($[M/H] = -0.23$). For this model, the distributions of the bar (red dashed line) and the thick bulge (red dotted line) are shown separately in the lower panel of Fig. 12. The bar stars reproduce the metal-rich peak of the observed MDF relatively well. However, the two components are not separated in metallicity as much as they are in the observations. If the

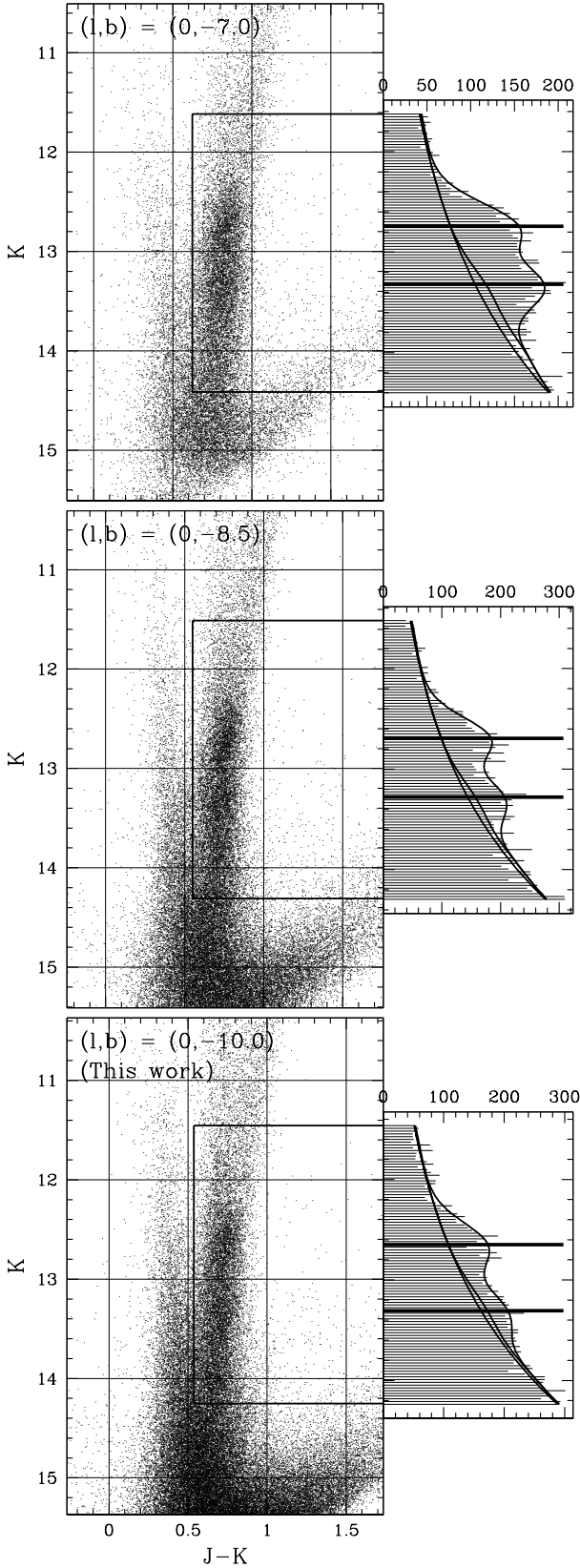


Fig. 11. Colour-magnitude diagrams of fields at $(l, b) = (0^\circ, -7.0^\circ)$ (top panel), $(l, b) = (0^\circ, -8.5^\circ)$ (middle panel), and $(l, b) = (0^\circ, -10.0^\circ)$ (bottom panel). For each field, a magnitude histogram of the stars in the thick box in the CMD is shown in the right hand panel, including a fit to the double RC, the RGB bump, and the underlying distribution of RGB stars. The thick horizontal bars in the magnitude histograms mark the peak magnitudes of the two RCs.

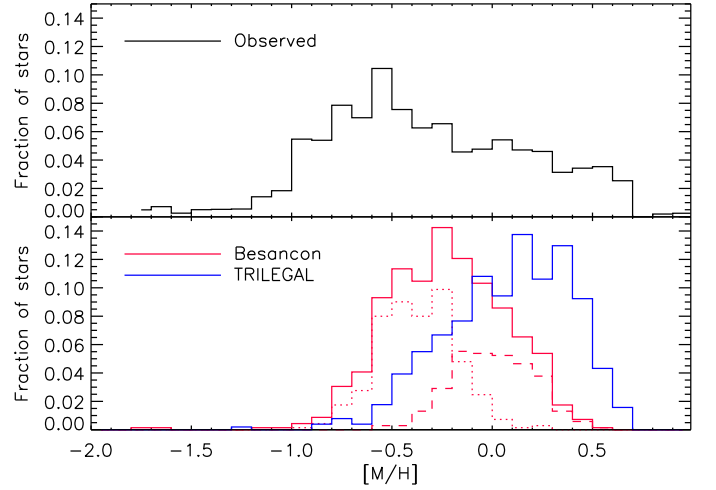


Fig. 12. Comparison of the observed MDF corrected for sampling effects (upper panel), with the ones predicted by the Besançon and TRILEGAL models in the selection region (lower panel). The histograms are normalised to the same area. In the lower panel, the red dotted line shows the MDF of “thick bulge” stars in the Besançon model, whereas the dashed red line is the one for the bar component.

bulge component in the Besançon model was shifted to lower metallicities by 0.2 to 0.3 dex, it would very nicely reproduce the metal-poor peak in the observed MDF (cf. Sect. 4.7.1). We remind that these stellar population synthesis models assume certain metallicity distributions for each Galactic component. Self-consistent chemical evolution models such as Ballero et al. (2007) are needed to do a detailed comparison.

4.5. α -element abundances

An important piece of evidence for the understanding of the GB population is the abundance of the α -elements because they convey information of the star formation history. In Fig. 13 we present the abundance of $[\alpha/\text{Fe}]$ as a function of the iron abundance $[\text{Fe}/\text{H}]$. The metal-rich and metal-poor stars also differ in this diagram: The metal-rich stars have clearly a lower over-abundance in the α -elements than the metal-poor ones. Among the metal-rich stars, most stars fall in the range $[\alpha/\text{Fe}] = +0.05$ to $+0.25$, while among the metal-poor stars many stars can be found at over-abundances of $+0.30$ dex and more.

Because of proximity to our field, we over-plot the abundances measured by Gonzalez et al. (2011a) in the field at $b = -12^\circ$. To convert the individual abundances to a combined $[\alpha/\text{Fe}]$ value, we computed the weighted mean of their Ca, Ti, Si, and Mg abundances, using as weight the contribution to the absorption in the synthetic spectrum that we applied in the determination of the α -abundances (Sect. 3.1.3). The match between our data and those of Gonzalez et al. (2011a) is not perfect. The over-abundances measured by Gonzalez et al. (2011a) are on average slightly higher than in our data, even though a shift was applied to our data to take into account a systematic offset (Sect. 3.1.4). It is also clear that there are many more metal-poor stars ($-1.5 \leq [\text{Fe}/\text{H}] \leq -0.5$) in our sample than in that of Gonzalez et al. (2011a), and also at the metal-rich end we find somewhat more stars than they do.

We also confirm the trend of decreasing α -element over-abundance with increasing metallicity, as was found already by a number of previous studies (e.g. Fulbright et al., 2007; Ryde et

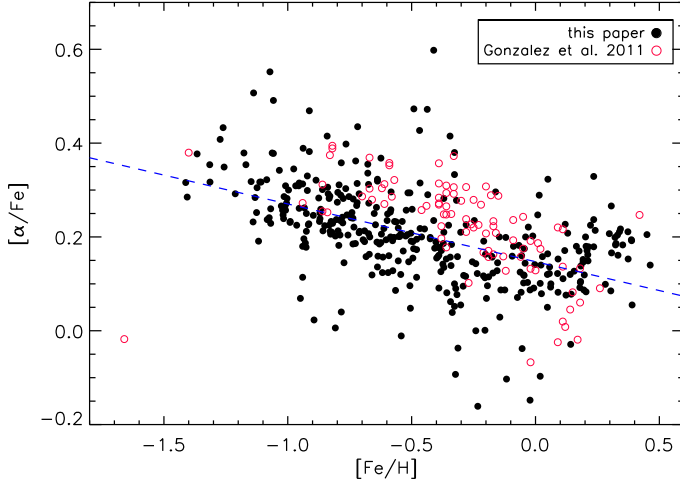


Fig. 13. Abundance of $[\alpha/\text{Fe}]$ as a function of $[\text{Fe}/\text{H}]$. Filled black circles: data from this study; open red circles: data of the field at $b = -12^\circ$ from Gonzalez et al. (2011a). The dashed line is a linear fit through the data of this paper.

al., 2010; Alves-Brito et al., 2010; Hill et al., 2011; Gonzalez et al., 2011a; Johnson C. et al., 2011; Bensby et al., 2010a). A linear regression including all sample stars yields a slope of -0.12 (dashed line in Fig. 13). The 1σ scatter around this slope is only ~ 0.08 dex, which suggests that it originates only from measurement error, not from real abundance scatter within the sample, at a given metallicity. At the high metallicity end, the trend of decreasing α -element over-abundance might be shallower or even reversed. This seems to disagree with the data of Gonzalez et al. (2011a) overplotted in Fig. 13, however. On the other hand, a flat trend with $[\text{Fe}/\text{H}]$ is also found in metal-rich, microlensed bulge dwarf stars for some α -elements, e.g. Ca, Ti, Si, and Mg (Fig. 10 of Bensby et al., 2011). Only oxygen is clearly found to continue its decrease at high metallicity. If this is a real feature or the result of uncertainties needs to be investigated with more precise line-by-line studies and larger samples, respectively.

4.6. Radial velocities

The RV distribution is an invaluable constraint on the nature of the GB, i.e. to decide whether it is a classical or a pseudo-bulge. The mean RV of our whole sample is $-8.3 \pm 3.8 \text{ km s}^{-1}$, with a velocity dispersion $\sigma_{\text{RV}} = 76.1 \pm 2.7 \text{ km s}^{-1}$ (Note: In the following, the quoted uncertainties in the mean velocity and the standard deviation of the distribution are always the purely statistical uncertainties.) The distribution of RVs of our sample stars is displayed in Fig. 14. No cold streams are obvious in our sample. Excluding the 50 foreground candidates identified in Sect. 2.3 by their high proper motion (and also the 10 stars for which no proper motion measurement was found), we get $\langle \text{RV} \rangle = -8.9 \pm 4.2 \text{ km s}^{-1}$ and $\sigma_{\text{RV}} = 77.1 \pm 3.0 \text{ km s}^{-1}$, hence no significant change.

We can compare our observed σ_{RV} to those of Babusiaux et al. (2010) and the BRAVA team (Howard et al., 2008, 2009). The comparison is done in Fig. 15, which is a reproduction of Fig. 7 of Babusiaux et al. (2010). We emphasise that the sample selection for the BRAVA survey, Babusiaux et al. (2010), and for the present study are quite different. From the BRAVA survey, only the results for fields along the bulge minor axis ($l \approx 0^\circ$) are shown. Our measurement of σ_{RV} is the lowest one in this figure, but within the error bar of the data point at $b = -12^\circ$ from

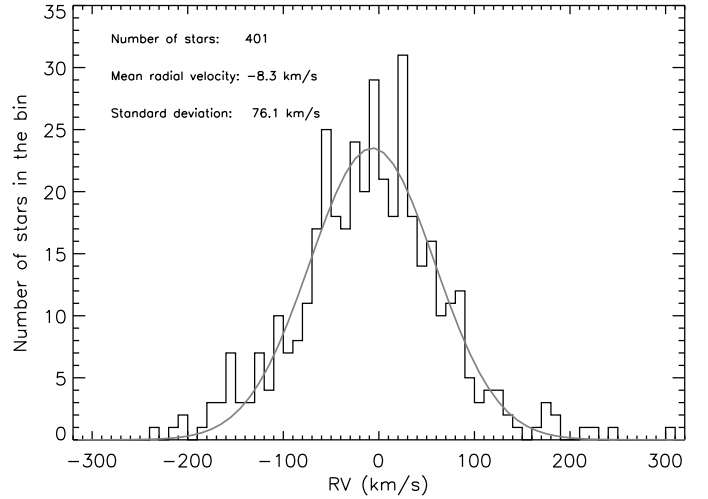


Fig. 14. Radial velocity distribution of our sample stars. The grey graph is a Gaussian fit to the data with mean and standard deviation as indicated in the figure.

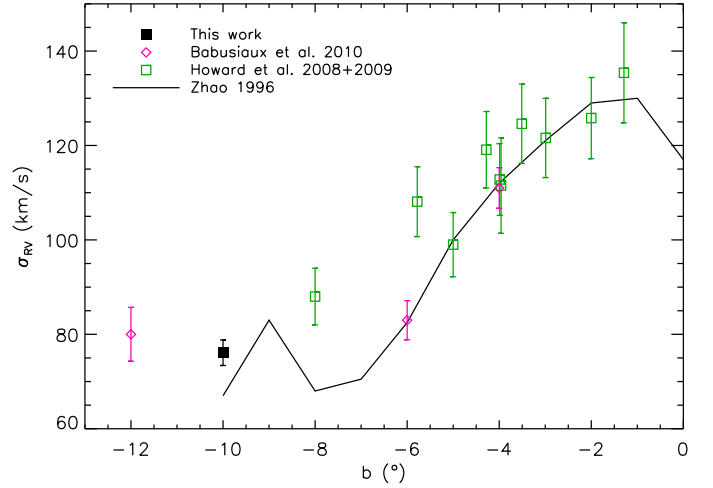


Fig. 15. Comparison of observed velocity dispersions as a function of Galactic latitude b along the bulge minor axis ($l = 0^\circ$) with the model of Zhao (1996). Cf. Fig. 7 of Babusiaux et al. (2010).

Babusiaux et al. (2010). Figure 15 also includes the prediction from the model by Zhao (1996), which is a “3D steady-state stellar dynamic model for the Galactic bar”, hence a pseudo-bulge model. The observed σ_{RV} as a function of b is well described by the model of Zhao (1996), except for the two BRAVA data points farthest from the Galactic plane. The σ_{RV} of our sample is only slightly higher than what is predicted by this model. Furthermore, our measurement is also in excellent agreement with the predictions of the pseudo-bulge model developed by Shen et al. (2010, their Fig. 2, lower right panel).

The kinematics of the RC stars is an important test for the understanding of the nature of the double RC feature. Figure 16 displays the RV distribution of the stars in the two RCs as defined in Sect. 2.2. The mean RVs are -10.4 ± 7.3 and $-6.0 \pm 6.1 \text{ km s}^{-1}$, and the standard deviations are 71.6 ± 5.2 and $74.1 \pm 4.3 \text{ km s}^{-1}$, respectively. Although the velocity dispersion of the faint RC is slightly larger than that of the bright RC, the two distributions are indistinguishable, within the error bars. To make this result more significant, we derived probabilities that a particular star

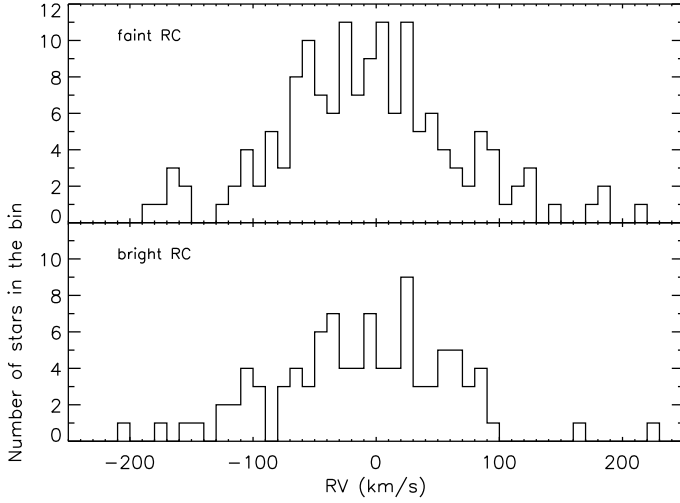


Fig. 16. Radial velocity distribution of the stars in the bright and faint RC, respectively.

Table 2. Radial velocity distributions of different sub-samples. The top group are the values measured from the observed sample, the bottom group are the values derived from ten simulation runs of the Besançon model (Robin et al., 2012).

Selection	N	$\langle RV \rangle$ (km s $^{-1}$)	σ_{RV} (km s $^{-1}$)
Observations			
whole sample	401	-8.3 ± 3.8	76.1 ± 2.7
$\mu < 20$ mas	341	-8.9 ± 4.2	77.1 ± 3.0
bright RC	96	-10.4 ± 7.3	71.6 ± 5.2
bright RC, weighted	96	-10.3 ± 7.3	71.3 ± 5.2
faint RC	150	-6.0 ± 6.1	74.1 ± 4.3
faint RC, weighted	150	-5.1 ± 6.1	73.5 ± 4.1
metal-rich third	128	-7.1 ± 4.6	52.3 ± 3.3
metal-poor third	128	-5.4 ± 8.0	90.6 ± 5.7
metal-rich pop. ¹	88	-6.1 ± 5.3	47.7 ± 5.6
metal-poor pop. ¹	198	-9.1 ± 6.4	90.3 ± 6.5
Besançon model			
whole sample	6933	-11.1 ± 0.9	77.8 ± 0.7
$\mu < 20$ mas	6555	-11.0 ± 1.0	79.6 ± 0.7
bright RC	1408	-10.0 ± 2.0	74.1 ± 1.4
faint RC	2802	-11.1 ± 1.5	80.9 ± 1.1
metal-rich third	2311	-13.1 ± 1.4	65.9 ± 1.0
metal-poor third	2312	-9.2 ± 1.8	87.2 ± 1.3

Notes. (1): Metal-rich and metal-poor population according to the Gaussian decomposition in Sect. 4.1.2.

belongs to either the front or back over-density (bright or faint RC). For this end we fitted two Gaussians (for the two RCs) and an exponential function (for the underlying RGB stars) to the magnitude histogram to derive these probabilities. This procedure was applied to a 40' diameter field to increase the statistics for a Gaussian fitting of the two RCs. Using these membership probabilities as weights, we get $\langle RV \rangle = -10.3 \pm 7.3$ km s $^{-1}$ and $\langle RV \rangle = -5.1 \pm 6.0$ km s $^{-1}$, and $\sigma_{RV} = 71.3 \pm 5.2$ km s $^{-1}$ and $\sigma_{RV} = 73.5 \pm 4.1$ km s $^{-1}$ for the bright and faint RC, respectively. Even in the weighted mean, the kinematics of the two RCs remain indistinguishable. Furthermore, a statistical t-test yields a probability of 64.2% that the two distributions are drawn from the same parent population.

The above discussed mean RVs and velocity dispersions of the different sub-samples are summarised in Table 2.

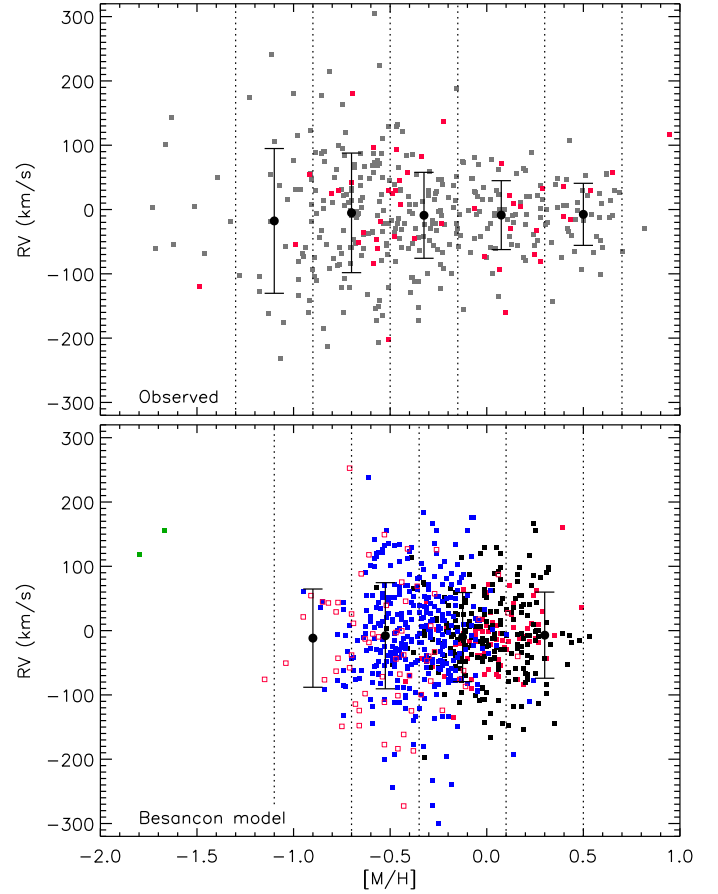


Fig. 17. Radial velocity versus metallicity. *Top panel:* observed sample stars. Foreground star candidates are represented by red squares, all other stars by grey squares. *Bottom panel:* simulated stars in the Besançon model (Robin et al., 2012). Blue squares represent the thick bulge, black squares the bar, filled red squares the thin disc, open red squares the thick disc, and green symbols represent the halo population. The over-plotted error-bar symbols in both panels show the mean and standard deviation of the RV over the metallicity range between the vertical dotted lines.

4.7. Combining kinematics with abundances

The upper panel of Fig. 17 shows how the sample stars distribute in the RV vs. [M/H] plane. It is immediately clear from this diagram that the RV distribution becomes broader with decreasing metallicity and that at low metallicity more extreme RV values are found than at high metallicity. This is also illustrated by the large over-plotted “error-bar” symbols, which show the mean RV and velocity dispersion over the metallicity range between the vertical dotted lines. The mean RV stays more or less constant, whereas σ_{RV} increases monotonically with decreasing metallicity. This is further evidence that there are two different populations present in our sample, each with its own velocity distribution. Whereas the increase in the velocity dispersion agrees with the results of de Propris et al. (2011), the lack of a trend of the mean RV with metallicity is in clear contrast to their results. This also holds if only the RC stars in our sample are considered. This is somewhat surprising because the field studied by de Propris et al. (2011) is only two degrees closer to the Galactic plane than our field, along the bulge minor axis. At this point we do not have an explanation for this discrepancy.

The metal-rich stars on the near side of the X (stars in the bright peak in the upper panel of Fig. 10) may be expected to differ in their mean radial velocity from those on the far side (faint peak in Fig. 10). We find $\langle RV \rangle = +1.5 \pm 7.5 \text{ km s}^{-1}$ and $\sigma_{RV} = 53.4 \pm 5.3 \text{ km s}^{-1}$ for the 51 bright, metal-rich RC stars and $\langle RV \rangle = -10.7 \pm 8.2 \text{ km s}^{-1}$ and $\sigma_{RV} = 51.5 \pm 5.9 \text{ km s}^{-1}$ for the 39 faint, metal-rich RC stars, respectively (using a metallicity cut at $[M/H] \geq -0.2$ and the brightness criteria for the RCs of Sect. 2.2). The error bars on the mean RVs overlap, hence the difference is not significant. Note, however, that RGB/early AGB stars brighter than the RC located on the far side and stars fainter than the RC located on the near side will dilute any difference between these two groups. A still larger sample would be needed to confirm this difference in mean RV.

4.7.1. Comparison with the Besançon model

It is interesting to compare this result with the kinematics as provided by the simulations to see whether the BGM, based on a decomposition in several populations, mainly disc, bulge and bar in the central region, is in reasonable agreement with our data. The lower panel of Fig. 17 shows for comparison the distribution of simulated stars in the BGM in the RV vs. metallicity plane. The width of the RV distribution as well as the extreme RV values agree well with those in the observed sample. However, the trend of increasing velocity dispersion with decreasing metallicity is much smaller in the simulation than in the observations. The main reason for this is that the bulge population (blue symbols in the lower panel of Fig. 17), whose velocity dispersion is relatively large, is close in metallicity to the bar population (black symbols), which has a smaller velocity dispersion. If the bulge population in the Besançon model was shifted to lower metallicities by 0.2 to 0.3 dex, it would nicely reproduce this trend, and also bring the range of metallicities in the model closer to the observed range. This is in line with the conclusions drawn from the comparison of the MDFs (Sect. 4.4).

To compare the observed with the simulated velocity dispersions, and to decrease the Poisson noise in the model, we calculated ten simulation runs of the Besançon model for our field. From these ten simulations, we obtain 6933 stars in the selection area. The results of this exercise are summarised in the lower part of Table 2. The mean RV as well as the velocity dispersion of the simulation agree well with the observed values for the whole sample. Excluding stars with a total proper motion $\mu > 20 \text{ mas/yr}$, the velocity dispersion slightly increases in both observations and simulations. As discussed in Sect. 3.2.3, this selection by proper motion is very efficient in removing the foreground disc. This increase in velocity dispersion is not significant in the observed sample, but it is significant in the simulation. In Fig. 18 we show the histogram of the distribution of radial velocity from the simulations, with (dashed line) and without (solid line) the proper motion selection. As can be seen from this figure, the proper motion selection removes a cold (disc) component.

Table 2 also lists the mean RV and dispersions of the simulated bright and faint red clump sub-samples, as well as for the metal-rich and metal-poor 33.3% quantile. In both the observations and in the simulations the bright RC has a slightly smaller velocity dispersion; while this increase is again not significant in the observed sample, it is significant in the simulations. The reason for this probably is that, as already discussed in Sect. 4.3, the faint RC is more contaminated by stars from the metal-poor population, which has a higher velocity dispersion than the bar population, the probable carrier of the double clump feature.

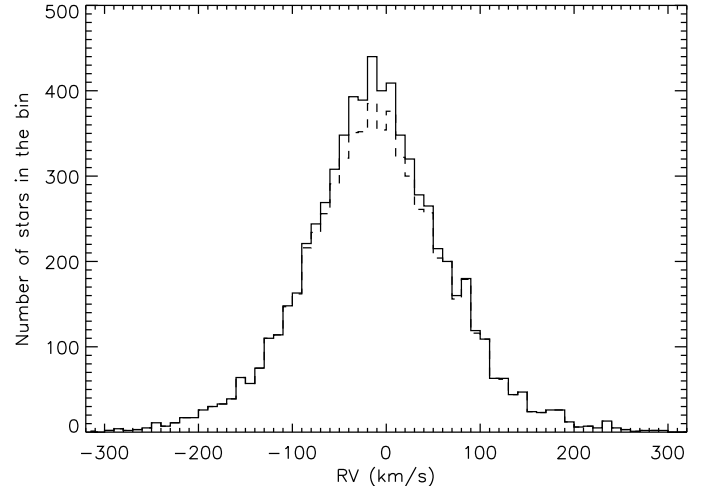


Fig. 18. Radial velocity distribution of stars in ten simulation runs of the Besançon model (Robin et al., 2012) for our field. The full line is for all stars in the selection region, the dashed line shows the distribution for stars with total proper motion $\mu < 20 \text{ mas/yr}$.

The metal-rich sample has a smaller velocity dispersion than the metal-poor one. This is due to the fact that the metal-rich one is dominated by the bar population, while the more metal-poor one is dominated by the bulge. The velocity dispersion of the metal-poor third of the simulation agrees nicely with the observed one (87.2 km s^{-1} to be compared with 90.6 km s^{-1} , see below). However, the metal-rich third has a larger dispersion in the simulations (65.9 km s^{-1}) than in the observed sample (52.3 km s^{-1}). As seen in the lower panel of Fig. 17, the metal-rich part of the sample is dominated by the bar, which follows Fux (1999) dynamics. But there is also a contribution from the disc, which is mainly removed using the proper motion selection. In the very low metallicity tail, there are a few halo stars and a noticeable contribution from the thick disc. It has, in our model, a smaller dispersion than the bulge, which has about the same metallicity. The velocity dispersion of the thick disc in the inner galaxy is not known and the simulation we are proposing here is just an attempt to extrapolate the thick disc as seen in the solar neighbourhood to the central region. Though, the dispersion we obtain for this intermediate and low metallicity bin is in very good agreement with the data.

We conclude that this new model, having both a flaring bar and a bulge component in the central region, explains very well the observed relation between the metallicity and the kinematics in this bulge field.

4.7.2. Comparison with the Fux model

The increase of σ_{RV} with decreasing metallicity is reminiscent of the results of Babusiaux et al. (2010), who also found a clear distinction in kinematics between the metal-poor and the metal-rich stars in bulge fields at different Galactic latitudes. In a reproduction of their Fig. 8, we show in Fig. 19 a comparison with the bulge dynamics as predicted by the 3D self-consistent N-body barred models of the Milky Way by Fux (1999). As in Babusiaux et al. (2010), σ_{RV} is plotted in different symbols for the complete sample (diamonds), the 33.3% metal-poor quantile (open downward-pointing triangles), and the 33.3% metal-rich quantile (filled upward-pointing triangles). We find $\sigma_{RV} = 52.3 \pm 3.3 \text{ km s}^{-1}$ for the metal-rich third of the sample

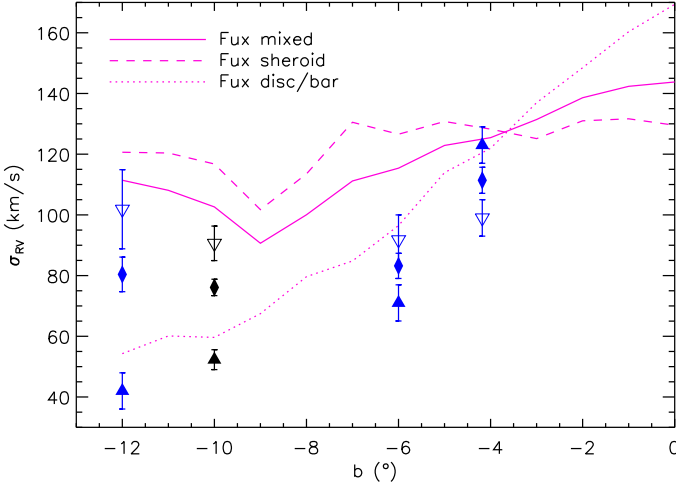


Fig. 19. Observed RV dispersions as a function of Galactic latitude b along the bulge minor axis, compared to the models of Fux (1999), cf. Fig. 8 of Babusiaux et al. (2010). The blue symbols are the data points from Babusiaux et al. (2010), the black symbols are from this work. The diamond symbol represents the velocity dispersion of the complete sample, while the open downward-pointing triangle represents the 33.3% metal-poor quantile and the filled upward-pointing triangle represents the 33.3% metal-rich quantile, respectively.

and $\sigma_{RV} = 90.6 \pm 5.7 \text{ km s}^{-1}$ for the metal-poor third (Table 2). By adding only one more data point at $b = -10^\circ$ we can put much more weight on the conclusions of Babusiaux et al. (2010). Within the error bars, σ_{RV} of the metal-poor quantile is constant throughout the bulge, from $b = -4^\circ$ to -12° . The spheroid model of Fux (1999) also predicts σ_{RV} to be fairly constant as a function of b , except for a dip around $b = -9^\circ$. However, the observed σ_{RV} is systematically lower than the σ_{RV} predicted by the spheroid model. The velocity dispersion of the 33.3% metal-rich quantile, on the other hand, decreases monotonically with increasing distance from the Galactic plane. This follows closely the prediction by the disc/bar model of Fux (1999), but except at $b = -4^\circ$ it is also always below the predicted value.

We must caution at this point that, while the definition of quantiles is a robust measure, the metallicity cuts will be at different absolute values, depending on the metallicity scale used in a given study and on the metallicity distribution in the different fields. We therefore also derived the RV dispersions of the two populations from the Gaussian decomposition done in Sect. 4.1.2. Assuming that both have Gaussian RV distributions, we find that the metal-poor population has $\langle RV \rangle = -9.1 \pm 6.4 \text{ km s}^{-1}$ with $\sigma_{RV} = 90.3 \pm 6.5 \text{ km s}^{-1}$, while the metal-rich population has $\langle RV \rangle = -6.1 \pm 5.3 \text{ km s}^{-1}$ and $\sigma_{RV} = 47.7 \pm 5.6 \text{ km s}^{-1}$ (Table 2).

4.7.3. Evidence for metallicity-dependent mass loss from the velocity dispersion of evolved stars

In Sect. 4.2 we speculated that the lack of metal-rich stars among the bright sample stars might be caused by strong, metallicity-dependent mass loss that preferentially removes metal-rich stars from the evolutionary pathes (the so-called AGB manqué). There is another, even stronger piece of evidence coming from the RV distributions of AGB stars and planetary nebulae (PNe) in the PG3 field that supports this explanation. RVs of Mira and semi-regular variables (SRVs) in the PG3 have been pre-

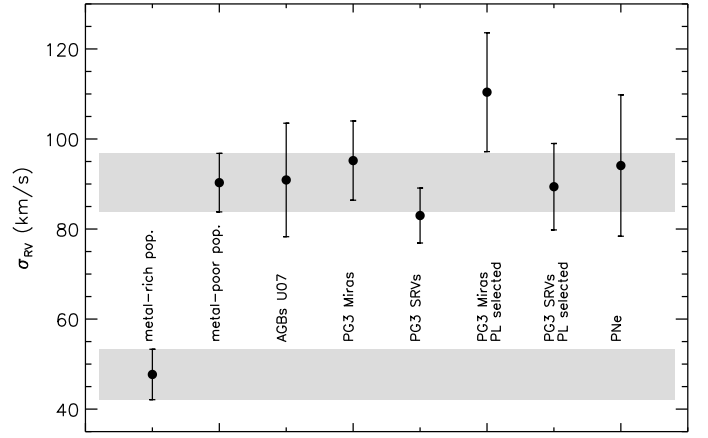


Fig. 20. Velocity dispersion of the metal-rich and metal-poor populations (Table 2), as well as of several samples of evolved stars towards the PG3 field: AGB stars from Uttenthaler et al. (2007, U07), Miras and SRVs from Schultheis (1998) without and with selection using a period - K -magnitude relation, and PNe from Durand et al. (1998). The grey shaded areas mark the range of uncertainty of the metal-rich and metal-poor population, respectively.

sented by Schultheis (1998) and Uttenthaler et al. (2007). The 27 AGB stars studied by Uttenthaler et al. (2007) by means of high-resolution UVES/VLT spectra have a velocity dispersion of $90.9 \pm 12.6 \text{ km s}^{-1}$. Schultheis (1998) found $\sigma_{RV} = 95.2 \pm 8.8 \text{ km s}^{-1}$ for 59 PG3 Miras and $\sigma_{RV} = 83.0 \pm 6.1 \text{ km s}^{-1}$ for 94 SRVs. If additional criteria based on the period - K -magnitude relation are applied to select only probable bulge members, these numbers change to $\sigma_{RV} = 110.4 \pm 13.2 \text{ km s}^{-1}$ (Miras, $N = 36$) and $\sigma_{RV} = 89.4 \pm 9.6 \text{ km s}^{-1}$ (SRVs, $N = 43$). Furthermore, we retrieved RV measurements of PNe from the compilation of Durand et al. (1998). Nineteen PNe were found within a search radius of 4° from the centre of our FLAMES field. Those 19 PNe have a velocity dispersion of $94.1 \pm 15.7 \text{ km s}^{-1}$. Although this last number is not highly significant owing to the small number of objects, it is clear that these velocity dispersions agree very well with the one determined for the metal-poor sub-population, but disagree with that of the metal-rich one. This statement is summarised in Fig. 20. We conclude from this that the AGB stars and PNe in the PG3 field descend mainly from the metal-poor sub-population. Or, to say it the other way round, we conclude that the metal-rich stars probably never evolve up to the AGB stage and beyond because they terminate their evolution before. This conclusion has also important consequences on the interpretation of the dual chemistry found in many bulge PNe (Guzman-Ramirez et al., 2011), a phenomenon which was previously assumed to be a consequence of high-metallicity PNe precursor stars (Perea-Calderón et al., 2009).

Apparently, there is a significant metal-rich population present out to $b \geq -10^\circ$, however it seems to be unable to produce highly evolved stars. Also the dearth of super-solar metallicity stars among M giants in fields close to the Galactic plane (Rich et al., 2007, 2012) may be caused by enhanced mass loss off metal-rich stars, in line with our result and interpretation. Finally, enhanced mass loss might also be required to understand the binary fraction of low-mass white dwarfs (Brown et al., 2011). A puzzle in this context is the presence of technetium-rich, long-period Mira stars towards the PG3 field (Uttenthaler et al., 2007), which suggest the presence of a younger and more massive ($M \approx 1.5 M_\odot$) population in the GB, but at the same

time carbon stars are extremely rare or even absent in the bulge (Blanco & Terndrup, 1989; Ng, 1997; Schultheis, 1998). This seems to be incompatible with the hypothesis of bulge AGB stars descending only from the old, metal-poor population. A solution to this problem could be that the Tc-rich AGB stars are the result of blue straggler evolution. Also problematic in this respect are the various selection effects that are certainly present on the AGB and PN samples in the GB, and only more detailed investigations, e.g. on the metal content of bulge AGB stars, can give more reliable answers.

A natural consequence of the loss of metal-rich stars by enhanced stellar winds would be that samples of bright M-type giants, as used by the BRAVA survey to probe the bulge velocity dispersion, could be biased towards *metal-poor* stars. In Sect. 4.6 we found that the observed σ_{RV} as a function of b is well described by the model of Zhao (1996), except for the two BRAVA data points farthest from the Galactic plane (Fig. 15). A bias towards low metallicity could be the reason why the σ_{RV} measured by BRAVA at large distances from the plane are systematically higher than the predictions by the Zhao (1996) model: at this Galactic latitude, the velocity dispersions of the metal-rich and the metal-poor populations differ considerably, thus a bias towards more metal-poor stars will yield an enhanced velocity dispersion.

5. Comparison of observed and simulated CMDs

Comparisons with observed CMDs are an important test of Galaxy models. The 2MASS all-sky catalogue is an ideal source for such constraints (see e.g. Robin et al., 2012). In Fig. 21 we provide a comparison for our field. No extinction correction was applied to the observed CMD. Rather, we applied the Marshall et al. (2006) 3D extinction model to both the TRILEGAL and BGM simulations. In addition, photometric errors in each filter of the order of those in the 2MASS catalogue were added to both the Besançon and the TRILEGAL simulation.

The CMD in this area of the sky is dominated by three sequences: a sequence on the blue side formed by main-sequence disc stars in the foreground, a vertical sequence formed by red clump stars distributing at various distances from the sun, and a red sequence formed by bulge stars, along which our selection of spectroscopic targets was made. These three sequences are most clearly resolved in the Besançon model (middle panel of Fig. 21), even though photometric errors of the same order of magnitude as in the 2MASS catalogue have been added to the simulated stars.

The two red clumps in the observed CMD at $J \sim 13^m3$ and $J \sim 14^m0$ are not well reproduced in the simulated CMDs for this field. This is not surprising for the TRILEGAL model, which uses a triaxial structure to describe the bulge. On the other hand, it has been shown that the flaring bar model developed by Robin et al. (2012) can reproduce the double clump feature, at least for a field at $(l, b) = (0^\circ, -7^\circ)$. The double clump feature is not obvious in this single simulation plotted here, but an inspection of the ten combined simulations (Sect. 4.7.1), which were calculated to reduce the Poisson noise, the two clumps are well discernible at J magnitudes of $\sim 13^m6$ and $\sim 14^m1$. Hence, while the faint RC is well matched by the Besançon model, the bright one is slightly underestimated in its brightness (e.g. due to an overestimation of its distance).

In the TRILEGAL CMD a vertical sequence of RC stars is dominating in the bulge, which is probably a result of the triaxial bulge structure seen almost end-on, such that the bulge RC stars distribute over a relatively large range of distances from

the sun. Furthermore, the number of stars in the disc sequence seems to be lower in the TRILEGAL simulation than it is in both the observed and the Besançon CMD. The number of stars in the CMDs of Fig. 21 is not normalised; star counts constitute an important test of population synthesis models (Girardi et al., 2005). In the colour and magnitude range of Fig. 21, the observed CMD contains 2148 stars, while the Besançon and TRILEGAL models contain 2456 and 1476 stars, respectively.

While some details in the simulated CMDs somewhat deviate from observed CMDs, it is clear that the Galaxy models have reached already a very high level of accuracy and can reproduce most of the stellar populations at least qualitatively.

6. Conclusions

We presented an analysis of spectra of ~ 400 red giant stars towards a field at $(l, b) = (0^\circ, -10^\circ)$. From these spectra, we derive metallicities, iron and α -element abundances, and radial velocities. It is the first study that presents a homogeneous analysis of stars on the upper and lower RGB of the Galactic bulge. These data, as well as photometric data from the 2MASS survey, are compared to predictions by the TRILEGAL (Girardi et al., 2005) and Besançon (Robin et al., 2012) models of the Galaxy. These models are also used extensively to interpret our observations.

The mean metallicity of the whole sample is $[M/H] = -0.34$, and the radial velocity dispersion is $\sigma_{RV} \sim 76 \text{ km s}^{-1}$. In this study we confirm the presence of two sub-populations in the bulge at peak metallicities that differ by ~ 0.9 dex. The peak metallicities are found at $[M/H] \sim -0.6$ and $\sim +0.3$, with roughly equal dispersions. The sub-populations have significantly different kinematics and α -element abundances: the metal-rich population has a narrow velocity distribution ($\sigma_{RV} \sim 50 \text{ km s}^{-1}$) and low α -abundances, whereas the metal-poor one has a broad distribution in radial velocities ($\sigma_{RV} \sim 90 \text{ km s}^{-1}$) and high α -abundances. The metal-rich population makes up $\sim 30\%$ of our sample. This confirms and fosters recent results by Babusiaux et al. (2010), Bensby et al. (2011), and Hill et al. (2011) in most aspects. Also the kinematic models of Zhao (1996) and Fux (1999) are confronted with our data, and good agreement is found.

Furthermore, we find support for the suggestion by Babusiaux et al. (2010) that the ratio in number of these two sub-populations is a function of angular distance from the Galactic plane, which explains the observed metallicity gradient. The new scheme in the Besançon Galaxy model explains well the features seen in this sample, with two populations, a flaring metal-rich bar and a more metal-poor classical or thick bulge, even though the mean metallicity of this thick bulge should be adjusted downward by 0.2 to 0.3 dex. The metallicity distribution simulated with the TRILEGAL model yields a clearly too high mean metallicity to fit our observations.

This study also presents the first medium-resolution, high-S/N spectra of stars belonging to the two red clumps of the bulge. A small difference in mean metallicity between the two RCs is attributed to selection effects. We find that the double RC might be entirely due to the metal-rich sub-population. The kinematic difference between the two RCs when measured with radial velocities alone is at most very small. Some difference in the mean radial velocity of bright and faint metal-rich RC stars is found, although a still larger sample would be needed to confirm that stars on the far side preferentially move faster towards us than the ones on the near side.

We also find indications that the metallicity distribution function of the bulge might depend on the evolutionary state of

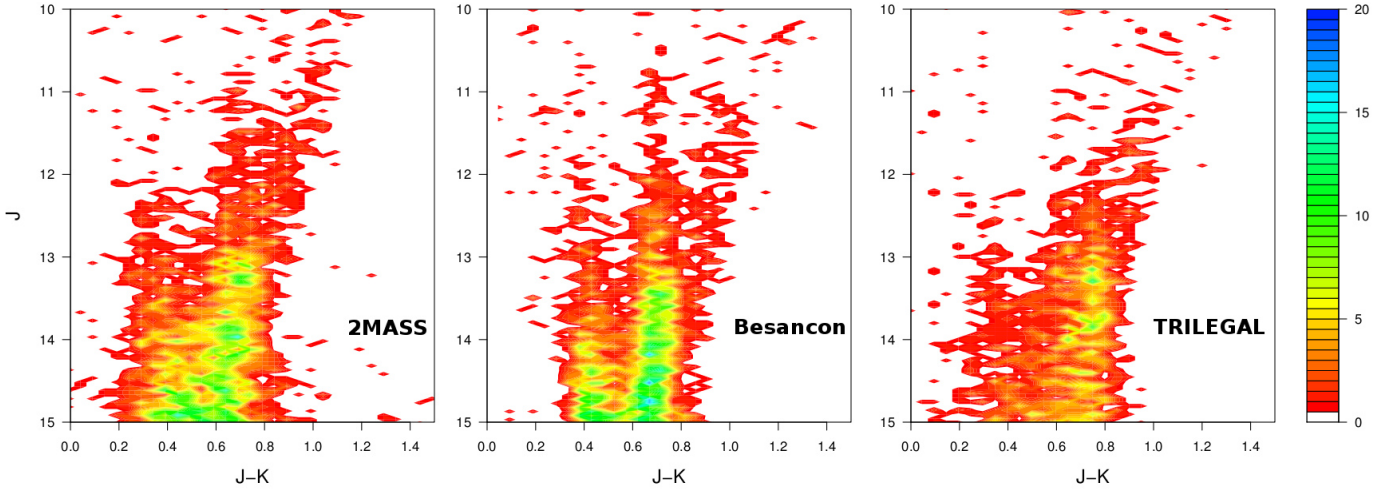


Fig. 21. Observed and simulated CMDs plotted as density maps. *Left panel:* observed CMD from 2MASS. *Middle panel:* simulated CMD from the Besançon model. *Right panel:* simulated CMD from the TRILEGAL model. The number of stars is not normalised. The scale on the right hand side illustrates to what colours the density of stars are connected in the diagrams.

the considered sample stars. In particular, there are fewer metal-rich stars present among the brighter, more evolved stars in our sample. Although this result could be a consequence of selection bias or the still limited number of stars in our sample, we interpret this as the result of strong mass loss that causes the most metal-rich stars to terminate their evolution before the most advanced states. A very robust indication for that comes from the fact that AGB stars and PN in the outer bulge have a velocity dispersion that agrees with that of the metal-poor population identified here, but clearly disagrees with that of the metal-rich population. We conclude, hence, that metal-rich stars might lose so much mass that they skip phases of post-main-sequence stellar evolution. This means that the selection of M giants in the BRAVA survey could be biased towards metal-poor stars. We also confirm the trend of decreasing α -element over-abundance with increasing iron abundance, as found in previous studies (e.g. Gonzalez et al., 2011a).

Our study also provides for an explanation how the existence of a dual bulge identified here and elsewhere can be reconciled with kinematic studies that conclude that the Milky Way bulge might be a pure pseudo-bulge (e.g. Shen et al., 2010). In our version of the Besançon model, the (thick or classical) bulge population has only 4% the mass of the bar, even when its contribution is significant when one moves away from the plane. Thus it is compatible with the result of Shen et al. (2010), which finds that the fraction of the classical bulge cannot be more than 8% of the disk mass. The pseudo-bulge dominates, but there is some space for a classical bulge, which we see in the data.

Acknowledgements. We thank Marica Valentini for pointing us to the abundance measurements of the RAVE survey and for helpful discussion. SU acknowledges support from the Austrian Science Fund (FWF) under project P 22911-N16 and from the Fund for Scientific Research of Flanders (FWO) under grant number G.0470.07. DMN was primarily supported by the NSERC grant PGSD3-403304-2011, and partially supported by the NSF grant AST-1103471. TL acknowledges support from the FWF under projects P 23737-N16 and P 21988-N16. The Besançon model simulations were executed on computers from the Utinam Institute of the Université de Franche-Comté, supported by the Région de Franche-Comté and Institut des Sciences de l’Univers (INSU). We acknowledge the support of the French Agence Nationale de la Recherche under contract ANR-2010-BLAN-0508-01OTP. This publication makes use of data products from the Two Micron All Sky Survey, which is a joint project of the University of Massachusetts and the Infrared Processing and Analysis Center/California Institute of Technology, funded by the National Aeronautics and Space Administration and the National Science Foundation.

References

- Aguerrí, J. A. L., Balcells, M., & Peletier, R. F., 2001, *A&A*, 367, 428
 Alves-Brito, A., Meléndez, J., Asplund, M., Ramírez, I., & Yong, D., 2010, *A&A*, 513, A35
 Aringer, B., Girardi, L., Nowotny, W., et al., 2009, *A&A*, 503, 913
 Athanassoula, E., 2005, *MNRAS*, 358, 1477
 Babusiaux, C., Gómez, A., Hill, V., Royer, F., Zoccali, M., et al., 2010, *A&A*, 519, A77
 Ballero, S. K., Matteucci, F., Origlia, L., & Rich, R. M., 2007, *A&A*, 467, 123
 Bensby, T., Zenn, A. R., Oey, M. S., & Feltzing, S., 2007, *ApJ*, 663, 13
 Bensby, T., Feltzing, S., Johnson, J. A., Gould, A., Adén, D. et al., 2010, *A&A*, 512, A41
 Bensby, T., Alves-Brito, A., Oey, M. S., Yong, D., & Meléndez, J., 2010, *A&A*, 516, L13
 Bensby, T., Adén, D., Meléndez, J., Gould, A., Feltzing, S., et al., 2011, *A&A*, 533, A134
 Bienaymé, O., Robin, A. C., Crézé, M., 1987, *A&A*, 186, 359
 Blanco, V. M., & Terndrup, D. M., 1989, *AJ*, 98, 843
 Boeche, C., Siebert, A., Williams, M., de Jong, R. S., Steinmetz, M., et al., 2011, *AJ*, 142, 193
 Brown, J. M., Kilic, M., Brown, W. R., & Kenyon, S. J., 2011, *ApJ*, 730, 67
 Caffau, E., Ludwig, H.-G., Steffen, M., et al., 2008, *A&A*, 488, 1031
 Castellani, M., & Castellani, V., 1993, *ApJ*, 407, 649
 Chiappini, C., Górny, S. K., Stasińska, G., & Barbuy, B., 2009, *A&A*, 494, 591
 Combes, F., & Sanders, R. H., 1981, *A&A*, 96, 164
 Combes, F., Debbauch, F., Friedli, D., & Pfenniger, D., 1990, *A&A*, 233, 82
 de Propris, R., Rich, R. M., Kunder, A., Johnson, C. I., Koch, A., et al., 2011, *ApJ*, 732, L36
 Durand, S., Aker, A., Zijlstra, A., 1998, *A&AS*, 132, 13
 Eggen, O. J., Lynden-Bell, D., & Sandage, A. R., 1962, *ApJ*, 136, 748
 Elmegreen, B. G., & Elmegreen, D. M., 2005, *ApJ*, 627, 632
 Elmegreen, B. G., Zhang, H.-X., Hunter, D. A., 2012, *ApJ*, 747, 105
 Fluks, M. A., Plez, B., The, P. S., de Winter, D., Westerlund, B. E., & Steenman, H. C., 1994, *A&AS*, 105, 311
 Fuhrmann, K., 2011, *MNRAS*, 414, 2893
 Fulbright, J. P., McWilliam, A., & Rich, R. M., 2007, *ApJ*, 661, 1152
 Fux, R., 1999, *A&A*, 345, 787
 Genzel, R., Newman, S., Jones, T., Förster Schreiber, N. M., Shapiro, K., et al., 2011, *ApJ*, 733, 101
 Girard, T. M., van Altena, W. F., Zacharias, N., Vieira, K., Casetti-Dinescu, D. I., et al., 2011, *AJ*, 142, 15
 Girardi, L., Bressan, A., Bertelli, G., & Chiosi, C., 2000, *A&AS*, 141, 371
 Girardi, L., Groenewegen, M. A. T., Hatziminaoglou, E., & da Costa, L., 2005, *A&A*, 436, 895
 Gonzalez, O. A., Rejkuba, M., Zoccali, M., Hill, V., Battaglia, G., et al., 2011a, *A&A*, 530, A54
 Gonzalez, O. A., Rejkuba, M., Zoccali, M., Valenti, E., & Minniti, D., 2011b, *A&A*, 534, A3
 Gomez, A. E., Grenier, S., Udry, S., Haywood, M., Meillon, L., et al., 1997, *Proceedings of the ESA Symposium “Hipparcos - Venice ’97”*, ESA SP-402,

- 621
- Guzman-Ramirez, L., Zijlstra, A. A., NiChuimín, R., Gesicki, K., Lagadec, E. et al., 2011, *MNRAS*, 414, 1667
- Haywood, M., 2008, *MNRAS*, 388, 1175
- Hinkle, K., Wallace, L., Valenti, J., & Harmer, D., 2000, “Visible and Near Infrared Atlas of the Arcturus Spectrum 3727-9300 Å”, (San Francisco: ASP)
- Hill, V., Lecureur, A., Gómez, A., Zoccali, M., Schultheis, M., et al., 2011, *A&A*, 534, A80
- Houdashelt, M. L., Bell, R. A., Sweigart, A. V., Wing, R. F., 2000, *AJ*, 119, 1424
- Howard, C. D., Rich, R. M., Reitzel, D. B., Koch, A., de Propriis, R., & Zhao, H., 2008, *ApJ*, 688, 1060
- Howard, C. D., Rich, R. M., Clarkson, W., Mallery, R., Kormendy, J., et al., 2009, *ApJ*, 702, L153
- Inoue, S., & Saitoh, T. R., 2012, *MNRAS*, 422, 1902
- Ivezić, Ž., Sesar, B., Jurić, M., Bond, N., Dalcanton, J., et al., 2008, *ApJ*, 684, 287
- Johnson, C. I., Rich, R. M., Fulbright, J. P., Valenti, E., & McWilliam, A., 2011, *ApJ*, 732, 108
- Johnson, J. A., Clanton, C., Howard, A. W., Bowler, B. P., Henry, G. W., et al. 2011b, *ApJS*, 197, 26
- Jørgensen, U. G., 1997, in *Molecules in Astrophysics: Probes and Processes*, ed. E. F. van Dishoeck (Kluwer), IAU Symp., 178, 441
- Kormendy, J., Kennicutt, R. C., 2004, *ARA&A*, 42, 603
- Kunder, A., Koch, A., Rich, R. M., de Propriis, R., Howard C. D., et al., 2012, *AJ*, 143, 57
- Kupka, F., Piskunov, N., Ryabchikova, T. A., Stempels, H. C., & Weiss, W. W., 1999, *A&AS*, 138, 119
- Lebzelter, T., Uttenthaler, S., Busso, M., Schultheis, M., & Aringer, B., 2012, *A&A*, 538, A36
- Lejeune, Th., Cuisinier, F., & Buser, R., 1997, *A&AS*, 125, 229
- Lejeune, Th., Cuisinier, F., & Buser, R., 1998, *A&AS*, 130, 65
- Marshall D. J., Robin A. C., Reylé C., Schultheis M., & Picaud S., 2006, *A&A*, 453, 635
- McWilliam, A., & Zoccali, M., 2010, *ApJ*, 724, 1491
- Meléndez, J., Asplund, M., Alves-Brito, A., Cunha, K., Barbuy, B., et al., 2008, *A&A*, 484, L21
- Nataf, D. M., Udalski, A., Gould, A., Fouqué, P., Stanek, K. Z., 2010, *ApJL*, 721, 28
- Nataf, D. M., Gould, A. P., Pinsonneault, M. H., & Udalski, A. 2012, submitted to *ApJ*, arXiv:1109.2118
- Ness, M., Freeman, K., Athanassoula, E., Wylie-de-Boer, E., Bland-Hawthorn, J., et al. 2012, accepted for publication in *ApJ*, arXiv:1207.0888
- Ng, Y. K., 1997, *A&A*, 328, 211
- Noguchi, M., 1998, *Nature*, 392, 253
- Noguchi, M., 1999, *ApJ*, 514, 77
- Norman, C. A., Sellwood, J. A., & Hasan, H., 1996, *ApJ*, 462, 114
- Norris, J., Bessell, M. S., Pickles, A. J., 1985, *ApJS*, 58, 463
- Ojha, D. K., Bienayme, O., Robin, A. C., Creze, M., & Mohan, V., 1996, *A&A*, 311, 4560
- Perea-Calderón, J. V., García-Hernández, D. A., García-Lario, P., Szczerba, R., Bobrowsky, M., 2009, *A&A*, 495, L5
- Raha, N., Sellwood, J. A., James, R. A., & Kahn, F. D., 1991, *Nature*, 352, 411
- Reylé, C., Robin, A. C., 2001, *A&A*, 373, 886
- Reylé, C., Marshall, D. J., Robin, A. C., & Schultheis, M., 2009, *A&A*, 495, 819
- Rich, R. M., Origlia, L., & Valenti, E., 2007, *ApJ*, 665, L119
- Rich, R. M., 2011, *Carnegie Observatories Astrophysics Series*, 5, 264
- Rich, R. M., Origlia, L., & Valenti, E., 2012, *ApJ*, 746, 59
- Robin, A. C., Reylé, C., Derrière, S., et al., 2003, *A&A*, 409, 523
- Robin, A. C., Marshall, D. J., Schultheis, M., & Reylé, C., 2012, *A&A*, 538, A106
- Ryde, N., Gustafsson, B., Edvardsson, B., Meléndez, J., Alves-Brito, A., 2010, *A&A*, 509, A20
- Saito, R. K., Zoccali, M., McWilliam, A., Minniti, D., Gonzalez, O. A., & Hill, V., 2011, *AJ*, 142, 76
- Schultheis, M., 1998, Ph.D. thesis, University of Vienna, Austria
- Schwenke, D., 1998, *Faraday Discussions*, 109, 321
- Shen, J., Rich, R. M., Kormendy, J., Howard, C. D., de Propriis, R., & Kunder, A., 2010, *ApJ*, 720, L72
- Skrutskie, M. F., Cutri, R. M., Stiening, S., et al., 2006, *AJ*, 131, 1163
- Thomas, D., Maraston, C., Bender, R., & Mendes de Oliveira, C., 2005, *ApJ*, 621, 673
- Twarog, B. A., 1980, *ApJS*, 44, 1
- Uttenthaler, S., Hron, J., Lebzelter, T., Busso, M., Schultheis, M., & Käufel, H. U., 2007, *A&A*, 463, 251
- Vanhollebeke, E., Groenewegen, M. A. T., & Girardi, L., 2009, *A&A*, 498, 95
- Zhao, H., 1996, *MNRAS*, 283, 149
- Zoccali, M., Renzini, A., Ortolani, S., Greggio, L., Saviane, I., et al., 2003, *A&A*, 399, 931
- Zoccali, M., Hill, V., Lecureur, A., Barbuy, B., Renzini, A., et al., 2008, *A&A*, 486, 177
- Zwitter, T., Siebert, A., Munari, U., Freeman, K. C., Siviero, A., et al., 2008, *AJ*, 136, 421

Table 3. Parameters and abundances of the sample stars.

No.	RA(J2000) deg.	Dec(J2000) deg.	<i>J</i> mag	<i>H</i> mag	<i>K</i> mag	<i>T</i> _{eff} K	RV km s ⁻¹	[M/H]	[Fe/H]	[α/Fe]	FG
(1)	(2)	(3)	(4)	(5)	(6)	(7)	(8)	(9)	(10)	(11)	(12)
001	276.814513	-33.589966	9.495	8.524	8.256	3465	+117.328	+0.94			*
002	276.544710	-33.787083	9.512	8.624	8.369	3697	+20.277	+0.21			
003	276.608107	-33.667065	9.516	8.615	8.298	3520	+76.484	-1.00			
005	276.918684	-33.751503	9.696	8.820	8.527	3629	+55.090	-1.12	-0.95	+0.07	
006	276.432104	-33.784958	9.926	9.061	8.704	3514	-29.587	+0.82			
007	276.714893	-33.891556	9.978	9.096	8.838	3698	+12.913	-0.56	-0.48	+0.11	
008	276.600416	-33.681347	10.007	9.121	8.891	3756	-135.108	+0.06	+0.05	+0.32	
009	276.807769	-33.757442	10.057	9.178	8.941	3749	+106.494	-1.10	-0.81	+0.01	
010	276.873765	-33.726830	10.098	9.183	8.932	3637	-128.768	-0.39	-0.41	+0.60	
011	276.817925	-33.649303	10.115	9.191	8.923	3578	-59.147	-0.76			
012	276.611791	-33.631435	10.170	9.330	9.094	3843	+74.703	-0.13	+0.06	+0.09	
013	276.506457	-33.723846	10.213	9.322	9.062	3681	+27.664	-0.06	+0.02	+0.29	
015	276.488172	-33.844830	10.232	9.400	9.158	3847	+85.083	-0.39	-0.30	+0.05	
016	276.682337	-33.955391	10.266	9.421	9.194	3845	+25.704	-0.27	-0.06	+0.08	
017	276.595604	-33.694199	10.406	9.574	9.312	3803	+50.134	-0.54	-0.32	+0.09	
018	276.592533	-33.625336	10.409	9.579	9.366	3914	-59.013	-0.70	-1.07	+0.55	
019	276.586978	-33.867764	10.470	9.639	9.438	3934	+178.014	-0.85	-1.15	+0.32	
020	276.704314	-33.794868	10.542	9.678	9.446	3794	+33.422	+0.29			*
021	276.653399	-33.955818	10.642	9.747	9.556	3815	+72.019	-0.56	-0.31	-0.04	
022	276.471245	-33.828197	10.657	9.769	9.520	3711	-80.548	+0.28			*
023	276.565931	-33.660713	10.690	9.821	9.542	3687	-42.688	+0.12			
024	276.667873	-33.869152	10.726	9.949	9.659	3857	-7.078	-0.14	+0.12	+0.08	
025	276.771326	-33.748791	10.735	9.924	9.721	3969	-131.548	-0.62	-0.29	+0.12	
026	276.566599	-33.576355	10.747	9.916	9.673	3849	+15.044	+0.02	+0.12	+0.17	
027	276.621730	-33.925117	10.779	9.943	9.708	3849	-0.464	+0.31	+0.38		
028	276.566492	-33.894100	10.807	10.005	9.774	3932	-78.865	-0.55	-0.19	+0.12	
029	276.632910	-33.850189	10.843	10.032	9.847	4008	+305.574	-0.58	-0.87	+0.23	
030	276.876718	-33.749680	10.911	10.121	9.909	3991	+13.784	-0.70	-0.93	+0.18	
031	276.833702	-33.646965	10.933	10.095	9.844	3808	-12.983	-0.68	-0.33	+0.05	
032	276.664170	-33.889168	11.002	10.132	9.895	3770	+59.999	+0.20			
033	276.608510	-33.775723	11.064	10.240	10.041	3953	+46.289	-0.25	-0.02	-0.15	
034	276.530697	-33.808578	11.077	10.243	10.056	3959	+72.605	-0.58	-0.60	+0.25	
035	276.734398	-33.905167	11.112	10.288	10.008	3775	+37.840	-0.17	-0.06	+0.16	
036	276.693013	-33.893147	11.119	10.247	10.060	3874	+110.060	-0.54	-0.34	+0.04	
037	276.455229	-33.789265	11.126	10.329	10.132	4017	+25.919	-0.06	-0.44	+0.29	
038	276.531016	-33.587563	11.157	10.323	10.122	3933	-105.342	-0.38	-0.03	+0.22	
039	276.476724	-33.652061	11.191	10.461	10.223	4074	-99.668	+0.03	-0.15	+0.13	
040	276.632713	-33.608341	11.204	10.397	10.238	4075	-213.279	-0.82	-1.06	+0.38	
041	276.611649	-33.623035	11.212	10.433	10.228	4037	+7.052	-0.40	-0.55	+0.20	
042	276.514543	-33.867790	11.212	10.396	10.256	4096	+3.906	-0.65	-0.80	+0.27	
043	276.545896	-33.910049	11.236	10.429	10.287	4109	-60.971	-0.41	-0.55	+0.20	
044	276.501519	-33.712631	11.270	10.456	10.228	3917	-66.401	-0.08	+0.18	+0.10	
045	276.497877	-33.881786	11.378	10.535	10.362	3969	+240.911	-1.11	-1.12	+0.19	
046	276.469519	-33.651062	11.403	10.619	10.362	3921	-1.719	-0.54	-0.34	+0.16	
047	276.718276	-33.890141	11.407	10.593	10.388	3957	+29.551	+0.05			
048	276.593535	-33.598366	11.415	10.584	10.345	3857	-9.884	+0.14	+0.23	+0.33	
049	276.751404	-33.686954	11.428	10.661	10.459	4065	+81.687	-0.06	-0.37	+0.21	
050	276.668148	-33.844818	11.433	10.578	10.353	3829	+29.158	-0.44	-0.12	-0.10	
051	276.897946	-33.802887	11.446	10.612	10.445	3992	-53.729	-0.83	-1.01	+0.26	
052	276.827522	-33.672203	11.457	10.650	10.435	3952	-28.859	+0.00			
053	276.598353	-33.763283	11.464	10.658	10.412	3893	+16.198	-0.02	+0.20	+0.09	
054	276.753347	-33.748871	11.480	10.655	10.504	4049	+21.622	-0.74	-0.92	+0.23	
058	276.763338	-33.726757	11.555	10.775	10.634	4167	-133.305	-0.97	-1.07	+0.26	
060	276.814847	-33.799526	11.592	10.814	10.653	4126	+19.204	-0.64	-0.79	+0.18	
061	276.745468	-33.614552	11.610	10.791	10.615	4011	-206.421	-0.56	-0.75	+0.24	
065	276.767964	-33.723507	11.682	10.895	10.664	3961	-59.417	+0.60			
067	276.764757	-33.714439	11.695	10.914	10.713	4036	-42.029	-0.33	-0.38	+0.13	
069	276.732436	-33.691238	11.750	10.953	10.767	4035	+28.948	-0.30	-0.43	+0.20	
070	276.809016	-33.594540	11.763	10.955	10.743	3957	-54.899	-0.19	-0.20	+0.00	
072	276.594486	-33.730743	11.791	11.111	10.937	4325	-52.206	-0.52	-0.59	+0.20	
073	276.836739	-33.717419	11.816	11.071	10.883	4139	-56.535	-0.28	-0.39	+0.16	
075	276.910260	-33.767544	11.837	11.034	10.873	4070	+45.375	-0.45	-0.59	+0.16	*
080	276.663676	-33.680828	11.956	11.185	11.002	4099	+67.611	-0.63	-0.80	+0.21	
081	276.598738	-33.673889	11.964	11.282	11.096	4294	-155.581	-0.12	-0.25	+0.23	
084	276.723840	-33.562702	11.989	11.339	11.120	4290	+29.832	+0.49	+0.21	+0.16	

Table 3. Continued.

No.	RA(J2000)	Dec(J2000)	<i>J</i>	<i>H</i>	<i>K</i>	<i>T</i> _{eff}	RV	[M/H]	[Fe/H]	[α /Fe]	FG
(1)	deg.	deg.	mag	mag	mag	K	km s ⁻¹	(9)	(10)	(11)	(12)
085	276.663499	-33.799038	12.006	11.199	11.069	4134	+58.329	-0.41	-0.51	+0.15	*
086	276.810910	-33.617214	12.009	11.269	11.096	4185	+9.035	+0.60	+0.22	+0.23	
088	276.843442	-33.804676	12.058	11.340	11.215	4343	+84.524	-0.42	-0.54	+0.12	
089	276.708411	-33.645660	12.060	11.331	11.179	4261	-58.044	-0.14	-0.30	+0.21	
096	276.728929	-33.625156	12.172	11.457	11.252	4171	+38.482	-0.48	-0.69	+0.21	
101	276.650041	-33.653530	12.257	11.553	11.355	4213	-123.588	-0.24	-0.34	+0.14	
102	276.603598	-33.725780	12.263	11.594	11.421	4352	-37.926	-0.61	-0.74	+0.25	
104	276.764294	-33.611069	12.270	11.528	11.326	4119	+23.454	+0.06	-0.21	+0.19	
107	276.796933	-33.752850	12.304	11.596	11.481	4392	+16.073	-1.03	-1.17	+0.35	
108	276.818554	-33.721001	12.315	11.546	11.354	4080	-55.377	+0.16	-0.05	+0.12	
110	276.831116	-33.661152	12.343	11.625	11.495	4334	-109.396	-0.97	-1.11	+0.32	
112	276.844085	-33.719276	12.386	11.681	11.584	4444	-3.301	-0.69	-0.89	+0.32	
115	276.876631	-33.669006	12.398	11.613	11.454	4115	-172.477	-0.36	-0.51	+0.29	
116	276.886129	-33.817890	12.401	11.716	11.560	4346	-54.145	-0.99	-1.08	+0.24	*
117	276.839217	-33.735954	12.407	11.626	11.535	4277	-141.307	-0.92	-1.00	+0.27	
118	276.605428	-33.607613	12.438	11.750	11.607	4380	+31.103	-0.99	-1.18	+0.38	
121	276.850407	-33.727764	12.470	11.850	11.667	4441	-2.194	-0.10	-0.32	+0.28	
123	276.733228	-33.686802	12.482	11.722	11.609	4278	-85.450	-0.76	-0.82	+0.23	
128	276.674814	-33.794342	12.520	11.823	11.717	4446	+32.514	-0.70	-0.81	+0.20	
131	276.862902	-33.842964	12.596	11.871	11.725	4277	-28.810	-0.37	-0.55	+0.22	
132	276.529376	-33.635666	12.607	11.953	11.827	4514	-159.866	-0.74	-1.06	+0.49	
133	276.754996	-33.640835	12.630	11.933	11.784	4341	+136.734	-0.22	-0.46	+0.20	*
136	276.670396	-33.678337	12.694	11.991	11.848	4342	-16.510	-0.50	-0.50	+0.21	
139	276.669257	-33.560745	12.724	12.024	11.849	4278	-8.143	+0.06	-0.16	+0.30	
142	276.592785	-33.609268	12.796	12.171	11.994	4454	-120.627				
143	276.720586	-33.791100	12.801	12.219	11.977	4391	-28.694				*
144	276.724865	-33.593685	12.806	12.156	12.024	4504	+47.662				
147	276.605327	-33.599644	12.834	12.130	12.014	4407	-13.128				
148	276.808190	-33.749828	12.835	12.127	11.988	4335	-40.138	-0.14	-0.36	+0.08	
154	276.884497	-33.711712	12.903	12.231	12.130	4521	-74.863	-0.00	-0.14	+0.09	
156	276.802245	-33.615543	12.915	12.209	12.115	4453	+5.379	+0.17	-0.04	+0.20	*
158	276.607949	-33.626446	12.936	12.308	12.179	4574	+47.731	-0.07	-0.12	+0.20	
159	276.506642	-33.859463	12.947	12.320	12.168	4514	-67.344	+0.55	+0.32	+0.18	
167	276.696311	-33.687943	12.992	12.354	12.170	4398	+16.036	-0.27	-0.64	+0.16	
169	276.585971	-33.583626	13.016	12.356	12.206	4434	-21.109	+0.02	-0.37	+0.28	
172	276.674085	-33.722809	13.036	12.399	12.232	4444	+62.310	+0.06	-0.09	+0.18	
178	276.673132	-33.740860	13.069	12.451	12.242	4385	-14.891	+0.46	+0.23	+0.18	
180	276.715472	-33.633411	13.078	12.449	12.266	4424	+57.926	+0.65	+0.39	+0.19	*
182	276.772886	-33.712326	13.085	12.412	12.316	4535	-44.163	-0.87	-1.00	+0.30	
183	276.791120	-33.629635	13.088	12.478	12.337	4584	-74.273	+0.39	+0.18	+0.17	
184	276.841313	-33.728474	13.093	12.437	12.271	4393	+13.471	+0.64	+0.37	+0.15	
186	276.721044	-33.780018	13.110	12.489	12.371	4618	+29.773	-0.70	-0.80	+0.24	
187	276.533345	-33.873089	13.112	12.435	12.314	4462	-142.788	+0.34	+0.12	+0.23	
188	276.753476	-33.945801	13.119	12.543	12.370	4585	+19.007	-0.20	-0.41	+0.18	
190	276.538801	-33.644936	13.134	12.484	12.360	4530	+11.192	+0.47	+0.23	+0.24	
191	276.627097	-33.841202	13.146	12.522	12.389	4569	-175.576	-1.05	-1.11	+0.32	
192	276.790756	-33.846645	13.151	12.493	12.363	4481	-8.106	-0.67	-0.83	+0.22	
193	276.717695	-33.835640	13.153	12.548	12.410	4605	+56.213	+0.15	-0.05	+0.17	
194	276.864580	-33.723576	13.154	12.547	12.417	4620	-33.430	-0.59	-0.74	+0.24	
195	276.694217	-33.601109	13.163	12.508	12.393	4537	-3.184	-0.68	-0.77	+0.30	
196	276.841761	-33.689163	13.167	12.539	12.385	4499	-44.337	-0.37	-0.52	+0.20	*
197	276.749744	-33.856068	13.171	12.572	12.406	4544	-22.102	-0.16	-0.33	+0.10	
198	276.638867	-33.930489	13.179	12.505	12.351	4381	+89.036	+0.23	+0.02	+0.08	
199	276.601595	-33.643906	13.190	12.594	12.394	4469	+55.281	+0.62	+0.39	+0.19	
200	276.910018	-33.774948	13.190	12.585	12.420	4527	-23.265	+0.20	-0.01	+0.20	
201	276.655418	-33.667728	13.192	12.617	12.458	4637	-12.106	+0.58	+0.34	+0.21	
202	276.600953	-33.920620	13.193	12.561	12.403	4480	-72.007	-0.65	-0.77	+0.14	
203	276.718361	-33.917198	13.194	12.505	12.362	4370	-112.531	-0.35	-0.50	+0.19	
204	276.651481	-33.734238	13.196	12.496	12.354	4351	-44.013	-0.36	-0.49	+0.17	
205	276.778831	-33.720421	13.203	12.613	12.452	4583	-66.094	-0.23	-0.32	+0.08	
206	276.529719	-33.594994	13.210	12.613	12.466	4613	+26.825	+0.69	+0.46	+0.14	
207	276.854131	-33.731907	13.221	12.595	12.447	4519	+62.408	-0.78	-0.97	+0.31	
208	276.628729	-33.743752	13.226	12.621	12.494	4642	-39.333	+0.24	+0.09	+0.08	
209	276.798530	-33.662918	13.233	12.540	12.415	4405	+95.619	-0.75	-0.86	+0.21	
210	276.836967	-33.769405	13.243	12.643	12.456	4484	+21.124	+0.26	+0.11	+0.11	

Table 3. Continued.

No.	RA(J2000)	Dec(J2000)	<i>J</i>	<i>H</i>	<i>K</i>	<i>T</i> _{eff}	RV	[M/H]	[Fe/H]	[α /Fe]	FG
(1)	deg.	deg.	mag	mag	mag	K	km s ⁻¹	(9)	(10)	(11)	(12)
211	276.756279	-33.788357	13.248	12.575	12.430	4404	-34.348	-0.54	-0.70	+0.19	
212	276.892143	-33.753590	13.248	12.670	12.487	4552	+21.790	+0.12	-0.05	+0.10	*
215	276.537753	-33.603622	13.256	12.649	12.491	4555	-119.873	-1.49			*
216	276.630558	-33.724087	13.258	12.652	12.484	4526	+38.871	+0.36	+0.18	+0.10	
217	276.611185	-33.719536	13.258	12.650	12.506	4586	+53.834	+0.62	+0.37	+0.21	
218	276.533293	-33.793808	13.263	12.630	12.449	4421	+25.411	+0.58	+0.33	+0.16	
219	276.490017	-33.791950	13.267	12.645	12.524	4614	+70.196	-0.68	-0.79	+0.29	
220	276.786346	-33.598869	13.267	12.685	12.496	4531	+36.370	+0.40	+0.20	+0.18	*
221	276.488605	-33.676846	13.277	12.662	12.508	4544	-68.765	-0.96	-0.98	+0.34	
222	276.765113	-33.566185	13.280	12.582	12.447	4371	+89.637	-0.84	-0.94	+0.11	
223	276.689571	-33.850536	13.283	12.596	12.483	4452	+63.721	+0.19	+0.06	+0.12	
224	276.530160	-33.772533	13.283	12.630	12.546	4630	-159.749	+0.10	-0.06	+0.12	*
225	276.490013	-33.854095	13.287	12.654	12.528	4568	-2.227	+0.47	+0.28	+0.10	
226	276.441487	-33.833378	13.287	12.601	12.440	4344	+86.733	-0.55	-0.71	+0.21	
227	276.460830	-33.865948	13.295	12.693	12.545	4593	-30.132	+0.42	+0.20	+0.12	
228	276.567606	-33.881664	13.305	12.729	12.573	4641	+5.293	+0.17	-0.05	+0.12	
229	276.488238	-33.744823	13.308	12.659	12.507	4457	-93.491	-0.90	-0.89	+0.02	
230	276.701957	-33.724052	13.317	12.670	12.492	4390	-15.167	+0.44	+0.21	+0.17	*
231	276.521504	-33.882675	13.318	12.634	12.517	4454	+87.725	-0.85	-0.94	+0.20	
232	276.701163	-33.812206	13.321	12.791	12.593	4650	+46.717	-0.24	-0.39	+0.16	
233	276.742927	-33.655430	13.327	12.768	12.577	4588	-33.817	+0.42	+0.20	+0.20	
234	276.817331	-33.599476	13.328	12.681	12.582	4598	+3.010	-0.17	-0.34	+0.06	
235	276.561797	-33.754608	13.331	12.760	12.590	4618	+2.381	+0.36	+0.18	+0.14	
236	276.811041	-33.747356	13.339	12.698	12.552	4485	-36.405	-0.64	-0.84	+0.42	*
237	276.543824	-33.638008	13.349	12.771	12.601	4601	-128.142	-1.17	-1.26	+0.35	
238	276.707179	-33.863255	13.363	12.721	12.560	4443	-48.485	+0.26	+0.09	+0.15	
239	276.514484	-33.893902	13.367	12.706	12.596	4534	-6.349	-0.66	-0.74	+0.18	
240	276.494178	-33.865170	13.374	12.671	12.545	4384	-45.410	-0.45	-0.61	+0.22	
241	276.691228	-33.652210	13.381	12.740	12.621	4563	+163.130	-0.75	-0.82	+0.21	
242	276.769980	-33.622349	13.400	12.785	12.587	4420	+37.049	+0.28	+0.14	+0.08	
243	276.445539	-33.820004	13.401	12.802	12.662	4626	-201.762	-0.51	-0.68	+0.34	*
245	276.458400	-33.680145	13.410	12.870	12.674	4637	-0.726				
246	276.732205	-33.735016	13.413	12.722	12.633	4506	-20.965	-0.26	-0.40	+0.19	
247	276.652760	-33.666142	13.415	12.859	12.647	4542	-12.734	+0.63	+0.34	+0.22	
248	276.663722	-33.563961	13.423	12.782	12.703	4680	-91.605	-0.82	-0.94	+0.39	
249	276.874535	-33.706005	13.432	12.805	12.675	4564	+20.002	+0.22	+0.05	+0.05	
251	276.814218	-33.891129	13.436	12.813	12.703	4630	-100.233	-0.18	-0.29	+0.09	
252	276.590433	-33.824047	13.447	12.815	12.625	4399	+14.280	-0.16	-0.37	+0.14	
253	276.698884	-33.720577	13.450	12.802	12.707	4608	-12.354	+0.28	+0.14	+0.12	
254	276.560443	-33.786304	13.457	12.905	12.659	4463	+47.473	+0.37	+0.19	+0.15	
256	276.885368	-33.847267	13.459	12.843	12.729	4637	+47.665	-0.61	-0.74	+0.28	
257	276.673226	-33.739399	13.464	12.896	12.744	4676	+53.227	+0.51	+0.30	+0.21	
258	276.509126	-33.638287	13.466	12.795	12.648	4414	+20.249	+0.22	+0.01	+0.25	
259	276.903426	-33.794418	13.475	12.812	12.641	4362	+0.338	+0.09	-0.07	+0.07	
260	276.856050	-33.636570	13.477	12.791	12.647	4375	-99.944	-0.31	-0.39	+0.09	
261	276.597652	-33.706051	13.478	12.889	12.705	4530	-56.387	+0.25	+0.06	+0.14	
262	276.627210	-33.776421	13.481	12.854	12.717	4552	-31.979	-0.74	-0.91	+0.47	
263	276.659752	-33.951805	13.489	12.884	12.727	4553	-5.578	+0.04	-0.12	+0.09	
264	276.545369	-33.932869	13.493	12.880	12.781	4701	-61.467	-0.25	-0.38	+0.17	
266	276.533760	-33.787659	13.505	12.874	12.744	4562	-68.790	-0.75	-0.83	+0.21	
267	276.616984	-33.586750	13.506	12.954	12.792	4699	-101.202	+0.59	+0.35	+0.18	
268	276.494876	-33.647800	13.515	12.919	12.794	4681	+71.564	+0.08	-0.07	+0.18	*
269	276.764459	-33.589680	13.518	12.940	12.784	4635	+69.289	-0.04	-0.15	+0.14	
270	276.614926	-33.938892	13.526	12.948	12.808	4680	+65.396	-0.69	-0.78	+0.23	
271	276.465499	-33.869881	13.526	12.857	12.692	4372	+29.413	+0.66	+0.39	+0.06	
272	276.827432	-33.753338	13.529	12.833	12.770	4559	-104.732	-1.17	-1.37	+0.38	
273	276.785331	-33.659843	13.538	12.873	12.710	4381	+223.568	-0.55	-0.66	+0.12	
274	276.842104	-33.732456	13.541	12.852	12.714	4381	-21.443	-0.28	-0.51	+0.10	
275	276.765440	-33.581825	13.554	12.999	12.817	4626	+68.660	-0.57	-0.67	+0.20	
276	276.728640	-33.949757	13.557	12.951	12.756	4446	-121.711	-0.71	-0.85	+0.22	
277	276.505794	-33.774723	13.561	12.941	12.782	4515	-51.159	+0.33	+0.05	+0.16	
278	276.714377	-33.724106	13.581	13.007	12.860	4672	+16.094	+0.29	+0.09	+0.12	
279	276.619384	-33.610786	13.591	12.968	12.842	4596	+50.290	-0.65	-0.73	+0.19	
280	276.699742	-33.801800	13.600	13.064	12.896	4722	-22.286	-0.43	-0.62	+0.37	
281	276.632739	-33.920406	13.601	12.931	12.843	4565	-74.670	+0.19	-0.02	+0.09	

Table 3. Continued.

No.	RA(J2000)	Dec(J2000)	<i>J</i>	<i>H</i>	<i>K</i>	<i>T</i> _{eff}	RV	[M/H]	[Fe/H]	[α /Fe]	FG
(1)	deg.	deg.	mag	mag	mag	K	km s ⁻¹	(9)	(10)	(11)	(12)
282	276.603736	-33.792931	13.606	13.010	12.886	4678	-59.064	-0.70	-0.79	+0.23	
283	276.839527	-33.652874	13.614	12.951	12.909	4717	-47.148	-0.57	-0.73	+0.36	*
284	276.724473	-33.882050	13.619	12.995	12.858	4555	-6.884	-0.38	-0.58	+0.19	
285	276.810256	-33.899017	13.632	12.985	12.875	4562	+24.234	-0.80	-0.90	+0.25	*
286	276.629095	-33.587997	13.646	13.024	12.914	4645	-104.407	-0.89	-0.93	+0.21	
287	276.860156	-33.865948	13.646	13.033	12.895	4578	+75.530	-0.57	-0.64	+0.19	
288	276.589341	-33.604183	13.659	13.078	12.939	4682	-63.114	-0.35	-0.48	+0.17	
291	276.787583	-33.871380	13.673	13.065	12.954	4673	-22.181	-0.53	-0.64	+0.14	
292	276.501441	-33.769341	13.689	13.075	12.971	4688	-60.436	-0.64	-0.75	+0.29	
294	276.807204	-33.744389	13.705	13.002	12.912	4469	-92.853	+0.49	+0.14	-0.03	
295	276.671937	-33.722317	13.712	13.142	13.001	4704	-7.833	+0.54	+0.32	+0.19	
296	276.472514	-33.777775	13.719	13.094	12.963	4578	+121.918	-0.44	-0.50	+0.19	
297	276.686566	-33.655930	13.744	13.148	13.021	4669	-110.334	-0.88	-0.92	+0.23	
298	276.665050	-33.818905	13.746	13.132	13.029	4684	+87.153	-0.58	-0.67	+0.27	
299	276.859868	-33.871136	13.748	13.085	12.995	4572	-105.991	-0.39	-0.50	+0.15	
300	276.442637	-33.752930	13.750	13.103	13.048	4737	-23.401				*
301	276.695536	-33.764545	13.751	13.160	13.029	4669	-68.258	-1.46			
302	276.749584	-33.841690	13.752	13.130	13.059	4752	-165.133	-0.54	-0.60	+0.19	
304	276.677892	-33.890118	13.758	13.194	12.984	4521	+54.041	-0.37	-0.50	+0.05	
305	276.676672	-33.567745	13.771	13.127	13.063	4715	-54.614	-1.62			
306	276.686629	-33.707558	13.777	13.146	13.024	4581	-57.854	-1.04	-1.13	+0.28	
307	276.712714	-33.944599	13.782	13.237	13.092	4760	-73.813	-0.01	-0.17	+0.12	*
308	276.542295	-33.749485	13.790	13.240	13.092	4746	-103.250	-1.28	-1.31	+0.35	
309	276.845057	-33.643093	13.797	13.196	13.031	4542	-7.766	-0.05	-0.20	+0.11	
310	276.737301	-33.623081	13.801	13.204	13.097	4724	+68.140	-0.59	-0.78	+0.28	
311	276.855065	-33.892948	13.813	13.230	13.106	4706	-10.062	-0.57	-0.63	+0.18	
312	276.805007	-33.749069	13.817	13.247	13.105	4695	-18.932	-1.12	-1.21	+0.29	
313	276.803927	-33.834248	13.821	13.261	13.126	4744	+29.782	-0.51	-0.65	+0.25	*
314	276.622601	-33.794971	13.822	13.150	13.024	4460	-60.428	+0.05	-0.20	+0.07	
315	276.821083	-33.773975	13.822	13.218	13.084	4618	+96.113	-0.59	-0.72	+0.31	*
316	276.689193	-33.710064	13.845	13.207	13.090	4575	+0.896	-0.07	-0.19	+0.10	*
317	276.527656	-33.798317	13.846	13.287	13.138	4716	-20.465	+0.31	+0.16	+0.13	
318	276.605035	-33.901566	13.846	13.198	13.094	4583	-8.413	+0.20	+0.06	+0.10	
319	276.676819	-33.581738	13.852	13.225	13.053	4460	-58.955	+0.02	-0.20	+0.16	
320	276.826131	-33.769146	13.853	13.137	13.051	4444	-41.389	-0.48	-0.62	+0.12	*
321	276.547129	-33.646622	13.857	13.271	13.155	4736	+11.187	+0.17	+0.05	+0.12	
322	276.625298	-33.608067	13.858	13.294	13.140	4687	-54.255	+0.13	-0.01	+0.09	
323	276.850420	-33.753113	13.859	13.172	13.081	4508	-52.017	-0.66	-0.78	+0.04	*
324	276.648919	-33.838467	13.868	13.295	13.114	4577	+29.848	+0.54	+0.30	+0.08	*
325	276.887809	-33.831329	13.871	13.297	13.117	4569	-84.110	-0.59	-0.69	+0.19	*
326	276.520313	-33.606983	13.871	13.248	13.174	4753	-13.705	-0.46	-0.47	+0.43	
327	276.743296	-33.606194	13.874	13.244	13.065	4431	+20.670	-0.05	-0.23	-0.16	
328	276.748212	-33.826157	13.875	13.305	13.185	4761	-29.200	-0.47	-0.55	+0.15	
329	276.494197	-33.811489	13.876	13.340	13.159	4690	+10.821	-0.72	-0.83	+0.28	
330	276.905290	-33.690044	13.879	13.243	13.114	4542	-21.543	-0.51	-0.64	+0.32	
331	276.661029	-33.805126	13.882	13.245	13.169	4696	-85.801	-0.24	-0.37	+0.19	
332	276.725178	-33.922646	13.894	13.301	13.118	4514	+74.659	-0.84	-0.94	+0.18	
333	276.803651	-33.785221	13.895	13.274	13.161	4630	-160.010	-0.93	-1.08	+0.32	
334	276.573211	-33.613113	13.897	13.384	13.189	4718	+30.030	-0.77	-0.72	+0.43	*
335	276.754422	-33.812862	13.899	13.284	13.177	4666	-3.150	-0.25	-0.39	+0.18	
336	276.775634	-33.868172	13.902	13.205	13.179	4661	-19.149	-0.55	-0.68	+0.35	*
337	276.609719	-33.899956	13.910	13.284	13.186	4663	+86.522	-0.65	-0.76	+0.25	
338	276.802770	-33.607288	13.910	13.270	13.182	4651	-31.855	+0.26	+0.02	+0.14	*
339	276.599163	-33.751358	13.916	13.369	13.197	4682	+21.543	+0.52	+0.31	+0.17	
340	276.862496	-33.881008	13.916	13.287	13.203	4688	-7.419	+0.15	+0.02	+0.10	
342	276.619675	-33.905045	13.925	13.343	13.216	4708	+123.234	-0.91	-1.02	+0.25	
343	276.694856	-33.562214	13.926	13.257	13.149	4519	+69.723				
344	276.586781	-33.832466	13.931	13.301	13.158	4528	+214.266	-0.81	-0.93	+0.26	
347	276.736184	-33.875690	13.949	13.316	13.213	4624	-45.041	-0.06	-0.25	+0.15	
348	276.578552	-33.619892	13.950	13.352	13.202	4600	+5.935	+0.41	+0.21	+0.15	
349	276.737919	-33.695145	13.956	13.350	13.207	4590	-65.841	+0.70	+0.45	+0.20	
350	276.456610	-33.796585	13.957	13.347	13.225	4647	-120.618	-0.51	-0.64	+0.26	
351	276.564966	-33.635128	13.960	13.423	13.248	4706	+128.623	-0.51	-0.71	+0.29	
353	276.861593	-33.801018	13.974	13.438	13.274	4728	+22.706	-0.73	-0.83	+0.29	
354	276.722013	-33.592499	13.974	13.376	13.238	4630	+46.922	-0.91	-1.07	+0.23	

Table 3. Continued.

No.	RA(J2000)	Dec(J2000)	<i>J</i>	<i>H</i>	<i>K</i>	<i>T</i> _{eff}	RV	[M/H]	[Fe/H]	[α /Fe]	FG
(1)	deg.	deg.	mag	mag	mag	K	km s ⁻¹	(9)	(10)	(11)	(12)
355	276.749304	-33.665966	13.975	13.357	13.210	4547	-58.417	-0.44	-0.53	+0.17	
356	276.762247	-33.786091	13.982	13.460	13.272	4702	+20.393	-0.41	-0.52	+0.26	
357	276.785991	-33.896404	13.985	13.341	13.224	4553	-84.393	-0.71	-0.82	+0.23	
358	276.833052	-33.776608	13.989	13.368	13.235	4572	-0.947	-0.70	-0.88	+0.28	
359	276.433122	-33.740566	13.989	13.411	13.292	4753	-32.267				
360	276.691675	-33.846764	13.993	13.347	13.275	4679	-38.991	-0.64	-0.80	+0.30	
361	276.705482	-33.740154	13.996	13.411	13.280	4687	+37.993	-0.65	-0.71	+0.21	
362	276.617111	-33.760021	13.996	13.410	13.278	4684	+7.110	-0.37	-0.54	+0.23	
363	276.493794	-33.799362	13.996	13.417	13.299	4750	+30.066	-0.89	-1.01	+0.31	
364	276.697108	-33.596195	13.996	13.460	13.297	4741	+49.761	-1.39	-1.41	+0.28	
365	276.575708	-33.577957	14.000	13.428	13.271	4656	+0.930	-0.85	-0.94	+0.31	
366	276.663677	-33.647522	14.002	13.400	13.306	4750	+12.679	-0.34	-0.45	+0.22	
367	276.779362	-33.567799	14.002	13.382	13.217	4495	+188.004	-0.16	-0.24	+0.00	
368	276.871279	-33.792786	14.006	13.428	13.318	4764	-35.508	-0.59	-0.76	+0.40	
369	276.580553	-33.632629	14.007	13.438	13.271	4634	-80.578	-0.47	-0.57	+0.23	
370	276.711834	-33.703365	14.013	13.394	13.306	4714	+48.722	-0.08	-0.23	+0.12	
371	276.743577	-33.898552	14.014	13.444	13.263	4581	-93.685	+0.07	-0.14	+0.03	*
373	276.441719	-33.814545	14.024	13.424	13.276	4601	+2.274	+0.28	-0.05	-0.04	
374	276.570897	-33.627617	14.025	13.431	13.228	4468	-16.193	+0.11	-0.24	+0.14	
376	276.747908	-33.773846	14.027	13.360	13.322	4718	-31.917	-0.26	-0.34	+0.18	
377	276.641959	-33.642696	14.027	13.439	13.293	4638	+9.039	+0.14	-0.00	+0.14	*
378	276.686341	-33.926971	14.032	13.484	13.341	4758	+119.348	-0.73	-0.87	+0.25	
379	276.867112	-33.799599	14.035	13.406	13.344	4755	+36.952	-1.07	-1.14	+0.23	
380	276.797940	-33.867813	14.041	13.329	13.276	4542	+10.755	-0.80	-0.87	+0.24	
381	276.615896	-33.679054	14.044	13.455	13.337	4718	-41.469	+0.57	+0.33	+0.20	
382	276.642599	-33.707905	14.051	13.414	13.319	4642	+29.732	-0.47	-0.59	+0.25	*
383	276.552809	-33.793800	14.052	13.441	13.273	4514	+58.636	-0.30	-0.37	+0.14	
384	276.767664	-33.790257	14.054	13.476	13.288	4542	-40.420	+0.44	+0.19	+0.15	
385	276.519644	-33.920509	14.060	13.538	13.278	4504	-29.684	+0.12	-0.09	+0.16	*
386	276.778487	-33.904800	14.063	13.482	13.386	4799	+7.124	-0.91	-1.01	+0.27	
387	276.738181	-33.939156	14.068	13.462	13.390	4797	+93.169	-0.47	-0.57	+0.20	*
388	276.529173	-33.642719	14.071	13.505	13.331	4624	-107.163				
389	276.805911	-33.751480	14.078	13.399	13.380	4737	+179.763	-0.69	-0.79	+0.31	*
390	276.654480	-33.594334	14.081	13.422	13.341	4621	-8.853	-0.70	-1.03	+0.27	
392	276.628139	-33.834789	14.097	13.540	13.394	4726	+7.430	-0.44	-0.60	+0.24	*
393	276.710695	-33.846008	14.100	13.400	13.312	4484	+84.567	-0.73	-0.93	+0.25	
394	276.689541	-33.778378	14.107	13.531	13.367	4616	+28.170	-0.26	-0.54	-0.01	
395	276.514699	-33.757675	14.110	13.464	13.352	4572	+143.624	-1.63			
396	276.694978	-33.943527	14.117	13.546	13.403	4689	+90.426	-0.85	-0.96	+0.22	
397	276.828208	-33.699005	14.118	13.473	13.418	4731	+31.582	-0.75	-0.83	+0.21	
398	276.515313	-33.784389	14.119	13.550	13.332	4493	-78.551	+0.20	+0.02	-0.10	
399	276.634575	-33.901833	14.126	13.579	13.433	4755	-52.671	-0.38	-0.50	+0.26	
400	276.829987	-33.806454	14.127	13.557	13.385	4605	-47.000	-0.69	-0.78	+0.24	
401	276.744083	-33.730270	14.129	13.516	13.358	4530	-64.671	+0.45	+0.21	+0.18	
402	276.879971	-33.675831	14.138	13.436	13.357	4500	+13.679	-0.65	-0.84	+0.31	
403	276.873784	-33.655762	14.143	13.553	13.461	4785	+181.139	-1.00	-1.13	+0.25	
404	276.750878	-33.678814	14.145	13.559	13.397	4593	-16.703	+0.50	+0.32	+0.20	
406	276.773448	-33.816742	14.159	13.602	13.453	4713	+89.280	-0.89	-1.03	+0.34	
407	276.538950	-33.857552	14.167	13.626	13.426	4617	-59.382	-0.94	-1.02	+0.26	
408	276.702749	-33.817944	14.168	13.557	13.489	4797	-91.236	-0.23	-0.31	+0.16	
409	276.578957	-33.705822	14.171	13.622	13.446	4665	+0.475	+0.07	-0.04	+0.14	
410	276.753490	-33.738415	14.173	13.552	13.448	4659	+24.100	+0.07	-0.28	+0.23	
411	276.836391	-33.686768	14.174	13.593	13.453	4669	+21.788	-0.30	-0.40	+0.15	
412	276.501238	-33.637436	14.174	13.595	13.412	4563	-161.418	-1.13	-1.27	+0.41	
413	276.662487	-33.626492	14.179	13.651	13.492	4778	+50.701	-0.16	-0.33	+0.38	
414	276.628673	-33.566936	14.185	13.516	13.421	4555	-5.715	-0.88	-0.99	+0.23	
415	276.534514	-33.915627	14.195	13.583	13.469	4660	+58.092	-0.59	-0.68	+0.16	
416	276.673953	-33.712120	14.197	13.610	13.502	4751	-111.533	-0.37	-0.48	+0.19	
417	276.561145	-33.898586	14.197	13.540	13.448	4592	+47.080	+0.41	+0.17	+0.18	
419	276.578991	-33.573586	14.206	13.587	13.472	4641	-41.636	-0.03	-0.32	-0.09	
420	276.687936	-33.576183	14.212	13.551	13.441	4535	-69.762	+0.25	+0.03	+0.16	*
422	276.852338	-33.874542	14.215	13.578	13.489	4650	-20.986	-0.46	-0.58	+0.26	
423	276.852706	-33.851723	14.232	13.667	13.550	4782	+45.436	-0.50	-0.58	+0.13	
424	276.886130	-33.787621	14.234	13.670	13.553	4785	+101.421	-1.66			
425	276.661265	-33.711018	14.238	13.657	13.487	4587	+23.665	-0.55	-0.67	+0.16	

Table 3. Continued.

No.	RA(J2000)	Dec(J2000)	<i>J</i>	<i>H</i>	<i>K</i>	<i>T</i> _{eff}	RV	[M/H]	[Fe/H]	[α /Fe]	FG
(1)	deg.	deg.	mag	mag	mag	K	km s ⁻¹	(9)	(10)	(11)	(12)
426	276.616342	-33.801567	14.238	13.734	13.527	4704	-107.099	-0.74	-0.84	+0.29	
427	276.858769	-33.890724	14.238	13.579	13.486	4575	-152.559	-0.36	-0.54	+0.21	
428	276.683750	-33.836472	14.242	13.685	13.528	4692	-70.446	-0.51	-0.62	+0.19	
429	276.794492	-33.592255	14.245	13.644	13.565	4796	+3.931	-1.73			
430	276.767692	-33.907009	14.247	13.673	13.511	4622	-154.454	-0.58	-0.67	+0.21	
431	276.561013	-33.621979	14.248	13.682	13.531	4692	+82.186	-0.34	-0.60	+0.12	*
433	276.801658	-33.837830	14.256	13.632	13.536	4670	-60.959	-0.57	-0.62	+0.21	*
434	276.665024	-33.724117	14.258	13.665	13.550	4713	-22.264	-0.23	-0.44	+0.47	*
435	276.768679	-33.857334	14.259	13.664	13.559	4730	+99.095	-0.77	-0.93	+0.19	
436	276.493553	-33.646214	14.263	13.713	13.588	4822	-50.196				*
437	276.827726	-33.647717	14.268	13.643	13.542	4655	-52.388	-0.68	-0.73	+0.22	
438	276.594804	-33.845116	14.271	13.742	13.515	4573	+5.719	+0.40	+0.20	+0.08	
440	276.631808	-33.564571	14.278	13.711	13.603	4819	+14.329	-0.84	-0.96	+0.31	
441	276.700830	-33.637337	14.281	13.799	13.534	4598	-18.383	-0.91	-1.12	+0.31	
443	276.727795	-33.730831	14.297	13.769	13.573	4663	-32.104	-0.85	-0.95	+0.26	
445	276.472846	-33.808666	14.310	13.670	13.574	4634	+73.543	-0.12	-0.33	+0.33	
446	276.438307	-33.774590	14.311	13.721	13.542	4544	-8.678	+0.65	+0.36		
447	276.777476	-33.775871	14.316	13.739	13.634	4786	-81.331	-0.98	-1.02	+0.24	
448	276.706230	-33.843826	14.316	13.735	13.588	4649	-20.233	+0.14	-0.03	+0.10	
449	276.798371	-33.735714	14.320	13.855	13.631	4765	+5.772	-0.74	-0.79	+0.20	
451	276.887413	-33.852146	14.324	13.738	13.636	4762	-184.313	-0.85	-1.06	+0.38	
452	276.661034	-33.891323	14.334	13.821	13.654	4794	-76.626	-0.79	-0.87	+0.26	
453	276.690616	-33.808006	14.336	13.754	13.596	4615	-48.148	-0.30	-0.43	+0.20	
454	276.698507	-33.939789	14.343	13.800	13.657	4773	+115.364	-0.98	-1.07	+0.24	
455	276.845583	-33.661392	14.344	13.746	13.667	4802	+65.842	-0.46	-0.47	+0.22	
456	276.593340	-33.672127	14.349	13.759	13.642	4719	-23.056	-0.32	-0.47	+0.31	
457	276.833423	-33.746063	14.353	13.767	13.581	4524	-23.375	-0.22	-0.36	+0.15	
459	276.615328	-33.576347	14.368	13.740	13.606	4561	+49.302	-0.79	-0.92	+0.30	
460	276.722855	-33.943268	14.391	13.838	13.708	4781	-73.249	-0.95	-0.99	+0.23	
461	276.834942	-33.635342	14.396	13.863	13.666	4643	-19.355	-1.33	-1.41	+0.32	
462	276.789630	-33.841022	14.400	13.855	13.727	4813	+4.985	-1.51			
463	276.467867	-33.749195	14.400	13.783	13.650	4595	-172.922	-0.57	-0.67	+0.31	
464	276.657623	-33.651539	14.406	13.786	13.632	4526	-67.065				
465	276.631871	-33.704411	14.417	13.879	13.739	4806	-121.778	-0.75	-0.92	+0.33	
466	276.861515	-33.729511	14.417	13.903	13.742	4806	-59.983	-1.71			
467	276.742712	-33.819698	14.422	13.889	13.745	4802	-9.504	+0.04	-0.15	+0.20	
468	276.511268	-33.792122	14.422	13.791	13.707	4696	+56.092	-0.91	-1.00	+0.28	
469	276.581345	-33.660347	14.425	13.834	13.711	4699	-44.438				
471	276.439088	-33.761520	14.447	13.839	13.738	4717	+35.018				
472	276.823834	-33.629124	14.464	13.925	13.731	4635	+131.626	-0.46	-0.56	+0.09	
473	276.670917	-33.612740	14.466	13.942	13.796	4833	+24.364	-0.49	-0.64	+0.32	*
474	276.547004	-33.669544	14.475	13.910	13.772	4733	-17.630	-0.28	-0.39	+0.18	
476	276.661846	-33.655987	14.491	13.900	13.829	4859	-29.627	-0.29	-0.41	+0.24	
477	276.853016	-33.748569	14.496	13.867	13.809	4768	-75.148	-0.89	-0.95	+0.31	
478	276.533779	-33.846905	14.501	13.982	13.812	4772	-38.002	-0.16	-0.35	+0.42	
481	276.777363	-33.671219	14.502	13.896	13.736	4543	-11.567	+0.39	+0.18	+0.09	*
482	276.573957	-33.858578	14.505	14.030	13.800	4722	-154.032	-0.57	-0.72	+0.27	
483	276.603613	-33.823669	14.506	13.932	13.766	4618	+31.359	-0.45	-0.65	+0.23	
484	276.594676	-33.571365	14.507	13.849	13.829	4810	-6.386				*
485	276.530138	-33.766701	14.511	13.876	13.792	4684	+129.335	-0.47	-0.58	+0.30	
486	276.865712	-33.679306	14.515	13.996	13.838	4801	-56.181	-0.52	-0.62	+0.16	
487	276.849420	-33.771736	14.519	13.847	13.786	4631	-141.982	-0.55	-0.72	+0.27	
488	276.598639	-33.744186	14.521	13.967	13.832	4771	-3.129	-0.04	-0.17	+0.16	
489	276.875366	-33.742172	14.521	13.810	13.769	4577	+73.034				
490	276.712242	-33.794239	14.531	13.928	13.856	4810	-2.514	-0.40	-0.56	+0.23	
491	276.751951	-33.710484	14.534	13.883	13.786	4593	-47.811	+0.59	+0.31	+0.27	
493	276.631945	-33.662464	14.538	13.956	13.862	4813	+54.638	-0.92	-1.01	+0.29	*
494	276.572343	-33.570671	14.542	13.939	13.812	4653	-28.906	-0.15	-0.28	+0.12	
495	276.548845	-33.833427	14.549	13.924	13.793	4575	+34.963	-0.02	-0.21	+0.12	
496	276.765063	-33.868202	14.555	13.990	13.859	4742	+77.859	+0.03	-0.18	+0.16	
497	276.830924	-33.896267	14.555	13.988	13.816	4612	-30.904	-0.44	-0.52	+0.20	
498	276.771491	-33.669971	14.559	13.951	13.817	4610	-23.933	+0.31	+0.13	+0.21	
499	276.633311	-33.762764	14.567	13.899	13.838	4650	+31.087	-0.96	-1.14	+0.51	
500	276.602649	-33.731819	14.567	14.041	13.883	4787	-1.571	-0.24	-0.35	+0.22	
501	276.858813	-33.772926	14.568	13.883	13.878	4759	+174.776	-1.23	-1.31	+0.32	

Table 3. Continued.

No.	RA(J2000)	Dec(J2000)	<i>J</i>	<i>H</i>	<i>K</i>	T_{eff}	RV	[M/H]	[Fe/H]	[α /Fe]	FG
(1)	deg. (2)	deg. (3)	mag (4)	mag (5)	mag (6)	K (7)	km s ⁻¹ (8)	(9)	(10)	(11)	(12)
503	276.436893	-33.808731	14.580	13.968	13.852	4659	-36.423	-0.48	-0.78	+0.36	
504	276.481768	-33.625542	14.581	13.971	13.872	4718	-67.245				
505	276.537031	-33.778503	14.584	14.036	13.893	4767	-9.908	-0.23	-0.49	+0.47	
506	276.502711	-33.686172	14.585	13.967	13.838	4604	-10.462				
507	276.736185	-33.691521	14.591	13.961	13.833	4566	-87.751	-0.77	-0.91	+0.38	
508	276.761504	-33.739830	14.594	13.971	13.862	4638	-231.533	-1.07	-1.26	+0.43	
509	276.856836	-33.670521	14.596	13.998	13.898	4737	-150.306	-0.56	-0.76	+0.20	
511	276.586662	-33.710934	14.606	13.974	13.869	4629	+106.628	+0.43	+0.24	+0.21	
512	276.620755	-33.646839	14.620	14.124	13.932	4776	-19.865				
513	276.868502	-33.816536	14.620	14.136	13.959	4851	+39.173	-0.23	-0.51	+0.29	
514	276.727030	-33.799290	14.624	14.014	13.922	4727	+42.665	-0.70	-0.86	+0.30	*

Notes. Meaning of the columns: (1): Target number in this programme; (2): Right ascension from 2MASS; (3): Declination from 2MASS; (4), (5), and (6): 2MASS *J*-, *H*-, and *K*-magnitude; (8): Effective temperature; (7): Heliocentric radial velocity; (9): General metallicity [M/H]; (10): Iron abundance [Fe/H]; (11): α -element abundance [α /Fe]; (12): Flag for foreground star candidates.